LAWRENCE
LIVERMORE
NATIONAL
LABORATORY

LLNL-TR-409660

# Development of a Safeguards Verification Method and Instrument to Detect Pin Diversion from Pressurized Water Reactor (PWR) Spent Fuel Assemblies Phase I Study

Y. S. Ham, S. Sitaraman

January 7, 2009

## Disclaimer



This work performed under the auspices of the U.S. Department of Energy by Lawrence Livermore National Laboratory under Contract DE-AC52-07NA27344.

**Final Report**
**LLNL-TR-409660**
**December 2008**

# Development of a Safeguards Verification Method and Instrument to Detect Pin Diversion from Pressurized Water Reactor (PWR) Spent Fuel Assemblies Phase I Study

Young S. Ham

and

Shivakumar Sitaraman

**E-Program, Global Security**

Lawrence Livermore National Laboratory

Table of Contents

Page

**List of Tables**

Page

## List of Figures

Page

## EXECUTIVE SUMMARY

A novel methodology to detect diversion of spent fuel from Pressurized Water Reactors (PWR) has been developed in order to address a long unsolved safeguards verification problem for international safeguards community such as International Atomic Energy Agency (IAEA) or European Atomic Energy Community (EURATOM). The concept involves inserting tiny neutron and gamma detectors into the guide tubes of a spent fuel assembly and measuring the signals. The guide tubes form a quadrant symmetric pattern in the various PWR fuel product lines and the neutron and gamma signals from these various locations are processed to obtain a unique signature for an undisturbed fuel assembly. Signatures based on the neutron and gamma signals individually or in a combination can be developed. Removal of fuel pins from the assembly will cause the signatures to be visibly perturbed thus enabling the detection of diversion. All of the required signal processing to obtain signatures can be performed on standard laptop computers.

Monte Carlo simulation studies and a set of controlled experiments with actual commercial PWR spent fuel assemblies were performed and validated this novel methodology. Based on the simulation studies and benchmarking measurements, the methodology developed promises to be a powerful and practical way to detect partial defects that constitute 10% or more of the total active fuel pins. This far exceeds the detection threshold of 50% missing pins from a spent fuel assembly, a threshold defined by the IAEA Safeguards Criteria. The methodology does not rely on any operator provided data like burnup or cooling time and does not require movement of the fuel assembly from the storage rack in the spent fuel pool.

A concept was developed to build a practical field device, Partial Defect Detector (PDET), which will be completely portable and will use standard radiation measuring devices already in use at the IAEA. The use of the device will not require any information provided by the operator or any prior knowledge of the spent fuel assembly. The device can also be operated without any movement of the spent fuel from its storage position. Based on parametric studies conducted via computer simulation, the device should be able to detect diversion of as low as ten percent of the missing or replaced fuel from an assembly regardless of the location of the missing fuel within the assembly, of the cooling time, initial fuel enrichment or burnup levels. Conditions in the spent fuel pool such as clarity of the water or boron content are also not issues for this device. The shape of the base signature is principally dependent on the layout of the guide tubes in the various types of PWR fuel assemblies and perturbations in the form of replaced fuel pins will distort this signature.

These features of PDET are all unique and overcome limitation and disadvantages presented by currently used devices such as the Fork detector or the Cerenkov Viewing Device. Thus, this device when developed and tested could fill an important need in the safeguards area for partial defect detection, a technology that the IAEA has been seeking for the past few decades.

*This work was performed under the auspices of the U.S. Department of Energy by Lawrence Livermore National Laboratory under Contract DE-AC52-07NA27344.*

## 1.0 INTRODUCTION

Various attempts have been made in the past two decades to develop a technology to identify a possible diversion of pins from a spent fuel assembly and to determine whether some pins are missing or replaced with dummy or fresh fuel pins. This aspect of the verification regime is known as partial defect detection. If diverted, this nuclear material, which is nuclear weapon-usable, could be the source of nuclear terrorism. Thus securing and monitoring one of the world's possible sources of nuclear terrorism is an essential part of the international safeguards regime.

With the discharge of over 10,000 metric tons of heavy metal from global reactors, storage pools in most countries are rapidly approaching their design limits. Some countries adopted a closed fuel cycle by reprocessing spent fuel and recycling MOX fuel whereas many of the countries opted for above ground interim dry storages for their spent fuel management strategy. Some countries like Finland or Sweden are already well underway in setting up a conditioning plant and a deep geological repository for spent fuel. For all these situations, transfers of spent fuel into containers are often needed and the subject spent fuel will attain a 'difficult-to-access' status. According to the IAEA Safeguards Criteria, the nuclear material should be verified prior to its becoming difficult-to-access by item counting, item identification where feasible and nondestructive assay (NDA) for gross and partial defects. The current detection requirement for partial defect tests for irradiated fuel assemblies should assure that at least half of the fuel pins (50%) are present in each assembly.

However, to date, there are no safeguards instruments that can detect partial defects that meet the requirements of the IAEA. The FORK detector system (FDET) [1] can characterize spent fuel assemblies using operator declared data, but the FORK detector cannot be applied for partial defect testing without use of the operator declared data [2]. Likewise, an emission computed tomography system has been used to try to detect missing pins from a SFA [3]. This has shown some potential for identifying possible missing pins but the capability has not yet been demonstrated, especially in an inexpensive, easy to handle setting for field applications. The Cerenkov viewing device is another instrument used in the field. However, it does not work well for fuel that has been cooled for a long time or low burnup fuel or in murky spent fuel pool conditions. It also has an issue with cases where the pins are missing in a random fashion since neighboring fuel pins of a missing one give off radiation potentially giving a false negative indication.

The novel Partial Defect Detector (PDET) methodology investigated in this study is intended to detect partial defects in Pressurized Water Reactor (PWR) spent fuel assemblies without relying on any input from the operator and without any movement of the fuel from the storage rack position. Unnecessary movement of fuel risks the occurrence of fuel handling accidents and is resisted by operators. The currently used system, FDET, cannot detect less than 50% of missing pins in an assembly. The PDET system is intended to detect as low as 10% of pins missing from an assembly. Finally, the PDET system will be completely portable for ease of use in the field and would consist of tiny neutron and gamma detectors that can be inserted into guide tubes present in the assemblies. The signals can be directly transmitted to a portable computer, like a laptop, and processed.

This report will discuss the various parametric studies performed using computer simulation on a unique signature of the PDET system and discuss the sensitivity of this signature to these parameters. The computer simulation model was benchmarked against measurements taken at KAERI in the Republic of Korea. The results of these benchmarking studies will also be presented in this report.

## 2.0 METHODOLOGY

Computer simulation studies were performed to develop the base signature for PDET and investigate the impact of various parameters on this signature. Several parameters were examined including multiple intra-assembly burnup patterns, soluble boron concentrations in the spent fuel pool, cooling time of the spent fuel, and initial enrichment. Most of the studies presented here use 14x14 PWR fuel as the basis of the simulation model. The study examines the sensitivity of the signature to these parameters both in single bundle and multi-bundle environments.

### 2.1 General Methodology

The isotopics for the spent fuel were obtained using ORIGEN-ARP [4] and only the most important isotopes were retained [5] for use in the subsequent analyses. The source spectra for both the neutrons (47-group structure) and gammas (20-group structure) were also obtained at the required cooling time. The isotopics and source spectra were used in the subsequent radiation transport calculation performed using MCNP [6], a 3D Monte Carlo radiation transport code.

### 2.2 Base Model

The base model selected was a lattice from the Kori-1 reactor [7]. The average initial enrichment of 3.8 weight% in $^{235}U$, was used to generate the isotopics and source spectra at various burnups present in the lattice. This particular lattice had an extreme burnup profile ranging from 20 MWd/t to 40 MWd/t. The base model assumed a cooling time of 10 years and no soluble boron in the pool.

The assembly was modeled as a 2D lattice that was isolated in the pool and surrounded by 30 cm of water. The Kori-1 lattice was an old 14x14 PWR model and had 16 guide tube locations. These guide tubes were originally modeled with water in them whereas they would be empty since during a measurement they would contain the detector array, which would displace the water that would normally be present when the assembly is stored in the spent fuel pool. The model was refined later to treat these locations as voids. The central instrument tube was modeled as water. The number of burnup levels found in the 179 active pins was approximated to nine distinct burnup levels. Figure 1 shows the burnup map with the red/orange regions having the highest burnup and the blue/green regions having the lowest burnups. The appropriate isotopics were input into the pins and source particles (neutron or gamma) were selected from the appropriate distributions depending on burnup. Two base runs were made: a coupled neutron-gamma run with a neutron source and a separate gamma run with a gamma source. Flux spectra were tallied in the 47-group structure for the neutrons and a 20-group structure for the gammas.

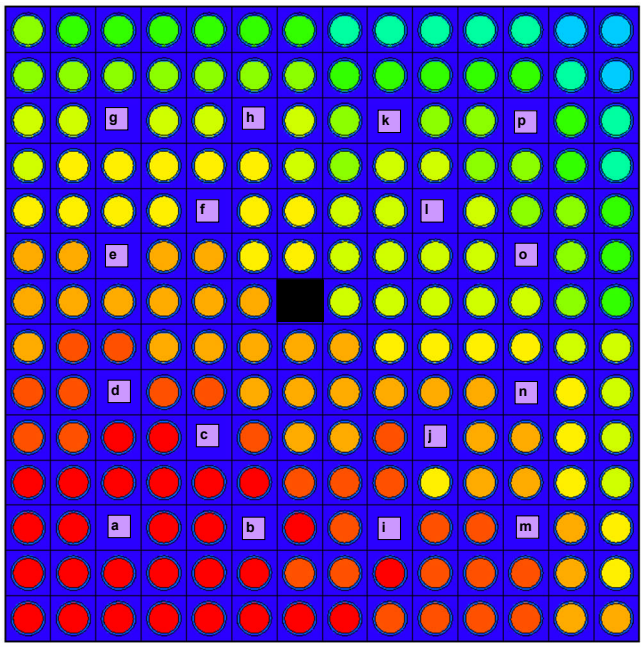


**Figure 1. Base MCNP Model**

### 2.3 Base Signature

The neutron signal is a very strong function of burnup. In low enriched fuel, the source term for neutrons increases as the power of 4-5 of the burnup. The neutron source term for cooling times greater than 2 years is principally dependent on the spontaneous fission of $^{244}$Cm [8]. The neutron source term is also dependent on initial enrichment and cooling time [8].

In contrast, the gamma source term is linearly dependent on burnup and comes mainly from cesium isotopes, and $^{137}$Cs in particular [8].

In a lattice with uniform burnup in every pin, the thermal neutron signal at each of the sixteen detector locations (guide tubes) will be purely geometry dependent, i.e. the location of the guide tube in the lattice. Symmetric locations will have the same thermal neutron signal. The gamma signal will be fairly constant at all locations. Thus, a unique signature, based mainly on geometry, can be obtained by taking the ratio of the gamma to thermal neutron signal at each guide tube and renormalizing them to the maximum of the sixteen ratios. This ratio will be referred to in the remainder of this document as the "normalized ratios". Thermal neutrons are defined as those neutrons with energies below the Cd cutoff of 0.4 eV.

When the burnup is non-uniform, this signature will still be fairly similar. Despite the strong dependence on the burnup, the thermal neutron signal at the guide tube locations itself turns out not to be such a strong function of burnup. This is mainly because the neutrons from spontaneous fission tend to migrate from the high density region (high burnup) to the lower density region (low burnup), thus diluting the strong dependence on burnup in individual pins. These neutrons also cause further fissioning in the pins leading to subcritical multiplication in the lattice. Therefore, the normalized gamma to thermal neutron ratio still maintains a strong dependence on the geometric layout of the guide tubes.

## 3.0 BASE RUNS

### 3.1 Base Runs with G23 at 10-year Cooling Time

In addition to the base case with the varying burnup, the 14x14 lattice case was run with the following four constant burnups: 37.3 MWd/kg, 33.2 MWd/kg, 29.0 MWd/kg, and 24.9 MWd/kg. Table 1 presents the normalized ratio for the four constant burnup cases as well as the base case, referred to as G23 (the ID of the assembly). The detector labels correspond to those shown in Figure 1.

**Table 1. Normalized Ratios from Base and Constant Burnup Cases**

| Detector | 10y G23 base | 10y 37.3 MWd/kg | 10y 33.2 MWd/kg | 10y 29.0 MWd/kg | 10y 24.9 MWd/kg |
|---|---|---|---|---|---|
| c | 0.911 | 0.915 | 0.914 | 0.91 | 0.906 |
| d | 0.932 | 0.933 | 0.93 | 0.927 | 0.926 |
| a | 0.975 | 0.999 | 1 | 1 | 0.999 |
| b | 0.923 | 0.933 | 0.932 | 0.932 | 0.928 |
| j | 0.919 | 0.923 | 0.919 | 0.916 | 0.916 |
| i | 0.925 | 0.934 | 0.932 | 0.929 | 0.93 |
| m | 1 | 1 | 0.998 | 0.998 | 1 |
| n | 0.945 | 0.932 | 0.935 | 0.931 | 0.927 |
| f | 0.931 | 0.905 | 0.903 | 0.903 | 0.897 |
| h | 0.939 | 0.933 | 0.929 | 0.928 | 0.927 |
| g | 1 | 0.999 | 0.999 | 0.999 | 0.998 |
| e | 0.94 | 0.931 | 0.927 | 0.929 | 0.926 |
| l | 0.923 | 0.919 | 0.911 | 0.912 | 0.906 |
| o | 0.932 | 0.934 | 0.93 | 0.93 | 0.928 |
| p | 0.993 | 0.999 | 0.997 | 0.999 | 0.999 |
| k | 0.932 | 0.934 | 0.931 | 0.927 | 0.927 |

From Table 1 above, it is clear that the maximum ratio occurs at locations a, g, m, and p. The minimum occurs at c, f, j, and l. This is as expected since the maximum ratio (i.e. with the lowest thermal neutron signal) would occur in the corner locations that have the fewest pins contributing to the signal. The peak thermal neutron signals would occur at the locations closest to the center. It should also be noted that the base case has a ratio of 0.975 at location ‘a’. This slight tilt in the signal compared to the four constant burnup cases is because of the burnup effect. It must be noted that location ‘a’ is surrounded by the highest burnup pins and despite the smearing effect discussed earlier, there is still an effect of the burnup gradient present in the lattice. In a more subtle effect, for the constant burnup cases, the location ‘f’ has a lower value than the other three central locations. This is because of the instrument tube (shaded black in Figure 1) is closer to location ‘f’ than it is to the others, thus enhancing the thermal neutron signal there.

Overall, these results suggest confirm that a unique signature, based mostly on the geometric location of the detectors rather than on other parameters, can be developed for each type of

PWR fuel product, i.e. 14 x 14, 15 x 15, 17 x 17 etc. Figure 2 shows the signature plotted in systematic way starting with the inner location and proceeding in a counter-clockwise manner for each set of four detector locations that are clustered together (e.g. c, d, a, b, etc.). Other patterns can be formed as well, but if this order is followed, the signal will always have the same shape as in Figure 2.

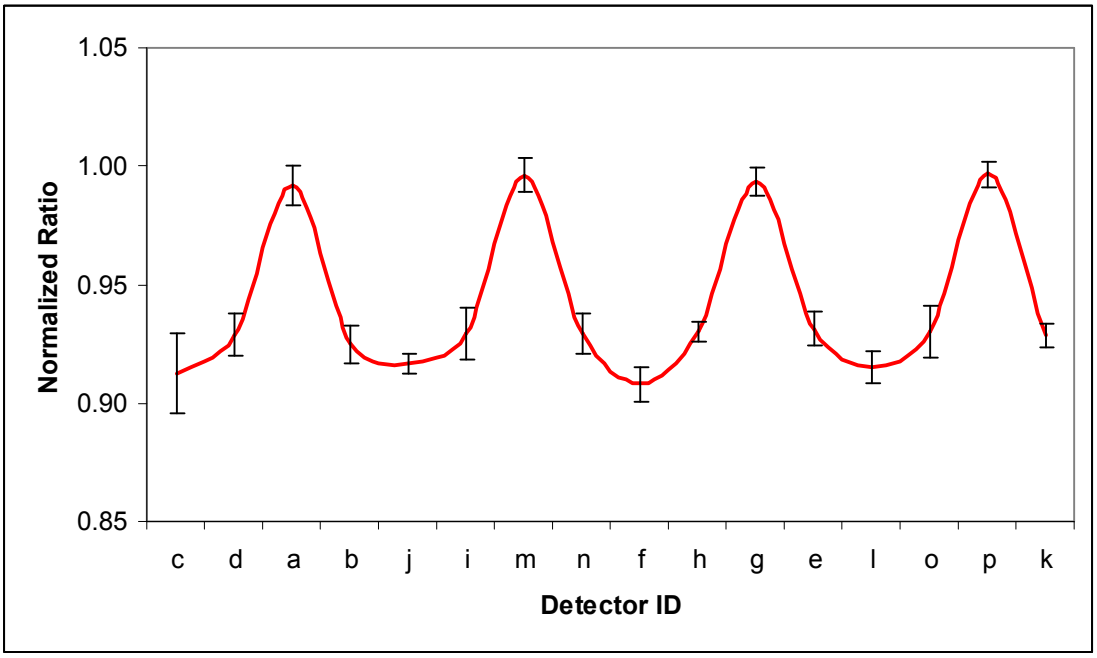


**Figure 2. Typical Signature**

The next few sections will deal with studies that examine the sensitivity of this signature to various parameters that potentially can impact it.

The statistical uncertainty at the 1-σ level for the ratio is between 1 and 2 percent. An error bar of 2% indicating the statistical uncertainty is shown in Figure 2. The error bars shown in the various sensitivity studies in the following sections are the spread of the data as a result of varying a specific parameter rather than the statistical uncertainty of each ratio. For the sake of clarity, the statistical uncertainties are not shown in these subsequent plots.

## 4.0 SENSITIVITY STUDIES WITH NO SOLUBLE BORON

### 4.1 Cooling Time

Sensitivity to cooling time is not expected to be very severe particularly since after about 2 years, the neutron and gamma sources tend to level off. Since the base case cooling time was 10 years, a second set of runs was made with a 5-year cooling time. All other parameters were kept constant. Table 2 presents results similar to those in Table 1 for the base case.

For the most part, it is seen that the results for the two cooling times agree within about 3% at the 2σ level. Figure 2 shows an average signal based on the ten cases presented in Table 1 and 2. Thus the signature is fairly invariant as a function of cooling time.

### 4.2 Different Burnup Profiles within a Lattice

A different fuel lattice from the same reactor (ID C15) with a less extreme burnup profile was also studied at a 10-year cooling time. This lattice exhibited a similar signature since this case would fall between the G23 base case and the constant burnup cases. Table 3 shows the comparison between the G23 and C15 cases.

**Table 2. Normalized Ratios from 5-year Cooling Time Cases**

| Detector | 5y G23 base | 10y G23 base | 5y 37.3 MWd/kg | 10y 37.3 MWd/kg | 5y 24.9 MWd/kg | 10y 24.9 MWd/kg |
|---|---|---|---|---|---|---|
| c | 0.895 | 0.911 | 0.924 | 0.915 | 0.913 | 0.906 |
| d | 0.91 | 0.932 | 0.933 | 0.933 | 0.925 | 0.926 |
| a | 0.946 | 0.975 | 0.997 | 0.999 | 0.996 | 0.999 |
| b | 0.9 | 0.923 | 0.928 | 0.933 | 0.922 | 0.928 |
| j | 0.918 | 0.919 | 0.917 | 0.923 | 0.909 | 0.916 |
| i | 0.908 | 0.925 | 0.933 | 0.934 | 0.93 | 0.93 |
| m | 0.989 | 1 | 1 | 1 | 1 | 1 |
| n | 0.947 | 0.945 | 0.924 | 0.932 | 0.92 | 0.927 |
| f | 0.927 | 0.931 | 0.906 | 0.905 | 0.897 | 0.897 |
| h | 0.948 | 0.939 | 0.931 | 0.933 | 0.926 | 0.927 |
| g | 1 | 1 | 0.988 | 0.999 | 0.987 | 0.998 |
| e | 0.932 | 0.94 | 0.935 | 0.931 | 0.93 | 0.926 |
| l | 0.926 | 0.923 | 0.917 | 0.919 | 0.904 | 0.906 |
| o | 0.932 | 0.932 | 0.936 | 0.934 | 0.929 | 0.928 |
| p | 0.99 | 0.993 | 1 | 0.999 | 1 | 0.999 |
| k | 0.935 | 0.932 | 0.932 | 0.934 | 0.925 | 0.927 |

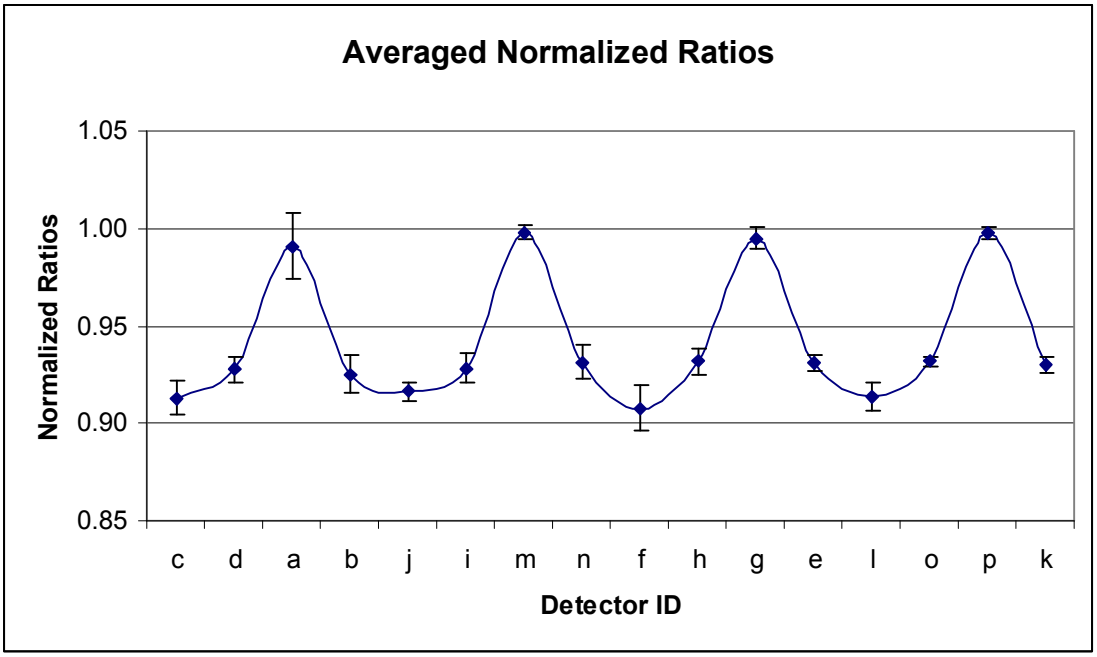


**Figure 3. Average Signal from 10- and 5-year Cooling Times**

The difference between the signals from the two lattices ranges from -0.02 to 0.04. A further example of differences between lattices of different varying enrichments will be presented later in this report. Figure 3 shows the average signal for 10 and 5 year cooling times.

**Table 3. Comparison of G23 and C15 Signals**

| Detector | G23 | C15 | Delta (difference) |
|---|---|---|---|
| c | 0.911 | 0.909 | 0.002 |
| d | 0.932 | 0.942 | -0.010 |
| a | 0.975 | 1 | -0.025 |
| b | 0.923 | 0.924 | -0.001 |
| j | 0.919 | 0.921 | -0.002 |
| i | 0.925 | 0.936 | -0.011 |
| m | 1 | 0.979 | 0.021 |
| n | 0.945 | 0.91 | 0.035 |
| f | 0.931 | 0.908 | 0.023 |
| h | 0.939 | 0.914 | 0.025 |
| g | 1 | 0.98 | 0.020 |
| e | 0.94 | 0.929 | 0.011 |
| l | 0.923 | 0.923 | 0.000 |
| o | 0.932 | 0.915 | 0.017 |
| p | 0.993 | 0.984 | 0.009 |
| k | 0.932 | 0.914 | 0.018 |

### 4.3 Enrichment Sensitivity

As discussed earlier, the neutron signal in spent fuel is affected by the initial enrichment of the fuel. In this study, in addition to the base case enrichment of 3.8 weight percent in $^{235}U$, cases with initial enrichment of 3 and 4.5% were examined. These cases were performed with a lattice of constant burnup of 33.2 MWd/kg. Table 4 presents the results and an average of the three cases. Figure 4 shows the signature comparisons. The signature is essentially insensitive to the initial enrichment as can be deduced from Table 4.

**Table 4. Comparison at Different Initial Enrichments**

| Detector | 10y 33.2 MWd/kg 3.8%enr | 10y 33.2 MWd/kg 3%enr | 10y 33.2 MWd/kg 4.5%enr | Average | Std. Deviation |
|---|---|---|---|---|---|
| c | 0.914 | 0.925 | 0.910 | 0.916 | 0.008 |
| d | 0.930 | 0.926 | 0.919 | 0.925 | 0.006 |
| a | 1.000 | 0.990 | 0.992 | 0.994 | 0.005 |
| b | 0.932 | 0.926 | 0.920 | 0.926 | 0.006 |
| j | 0.919 | 0.912 | 0.901 | 0.911 | 0.009 |
| i | 0.932 | 0.932 | 0.924 | 0.929 | 0.005 |
| m | 0.998 | 1.000 | 1.000 | 0.999 | 0.001 |
| n | 0.935 | 0.923 | 0.913 | 0.924 | 0.011 |
| f | 0.903 | 0.903 | 0.893 | 0.900 | 0.006 |
| h | 0.929 | 0.931 | 0.923 | 0.928 | 0.004 |
| g | 0.999 | 0.980 | 0.983 | 0.987 | 0.010 |
| e | 0.927 | 0.931 | 0.926 | 0.928 | 0.003 |
| l | 0.911 | 0.914 | 0.898 | 0.908 | 0.008 |
| o | 0.930 | 0.932 | 0.927 | 0.930 | 0.002 |
| p | 0.997 | 0.996 | 0.998 | 0.997 | 0.001 |
| k | 0.931 | 0.929 | 0.919 | 0.926 | 0.007 |

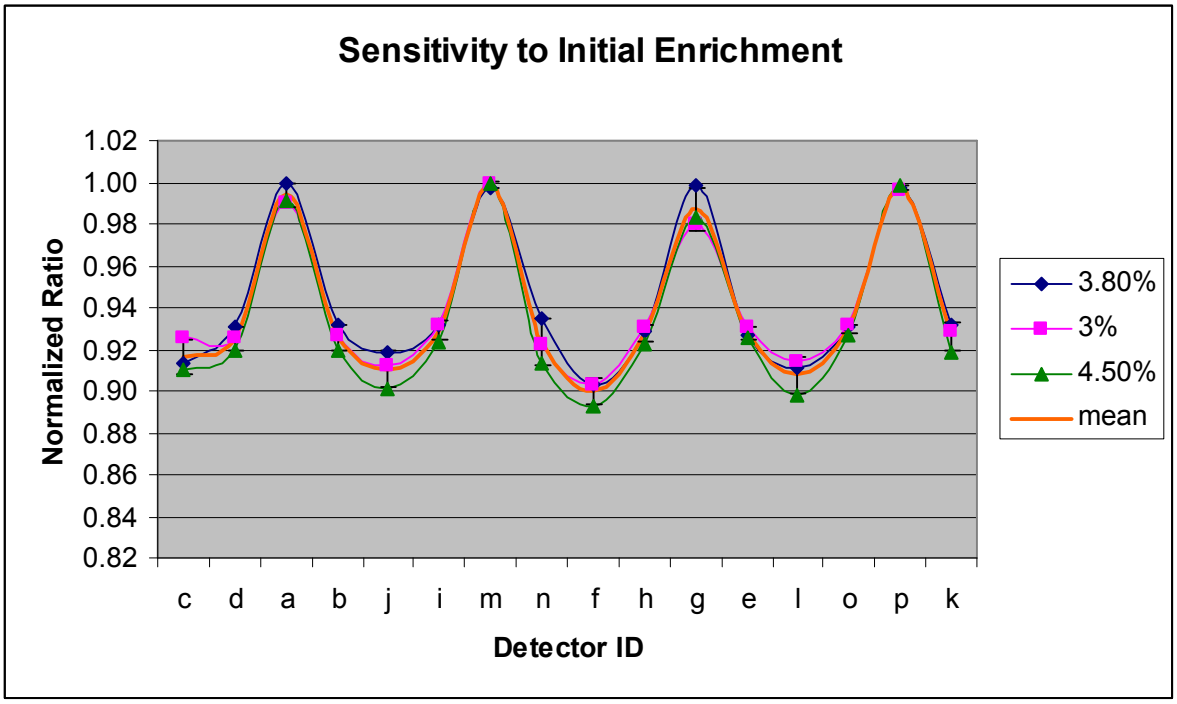


**Figure 4. Sensitivity to Enrichment**

### 4.4 Sensitivity to Water in the Detector Locations

When the actual measurements are made, the water in the guide tube locations will be replaced by the detector. Since the hardware in the detector will not occupy much of the space, the guide tube locations will be modeled as being empty. A study was conducted to determine the effect of replacing the water in the guide tubes with a void.

Table 5 presents the result of this study that shows minimal impact except at the center locations (~6%). These locations tend to see a larger number of thermal neutrons and the relative decrease of local moderation tends to have a larger impact on them. The corner ones on the contrary, see the smallest change. The relative change with and without water of the gamma signal for all locations is constant.

**Table 5. Effect of Water in the Guide Tubes**

| Detector | Average base-water | Base-no water | Ratio of Water/No Water |
|---|---|---|---|
| c | 0.911 | 0.968 | 0.94 |
| d | 0.932 | 0.963 | 0.97 |
| a | 0.975 | 0.971 | 1 |
| b | 0.923 | 0.95 | 0.97 |
| j | 0.919 | 0.973 | 0.94 |
| i | 0.925 | 0.953 | 0.97 |
| m | 1 | 1 | 1 |
| n | 0.945 | 0.973 | 0.97 |
| f | 0.931 | 0.996 | 0.94 |
| h | 0.939 | 0.961 | 0.98 |
| g | 1 | 0.994 | 1.01 |
| e | 0.94 | 0.977 | 0.96 |
| l | 0.923 | 0.974 | 0.95 |
| o | 0.932 | 0.955 | 0.98 |
| p | 0.993 | 0.995 | 1 |
| k | 0.932 | 0.961 | 0.97 |

## 5.0 STUDIES WITH SOLUBLE BORON

The studies in Section 4 were conducted with no soluble boron present in the spent fuel pool water. Soluble boron is typically present in PWR spent fuel pools. The presence of a strong thermal neutron absorber in the water will tend to make the thermal neutron signal more local thus enhancing the effect of burnup. This section deals with the several cases performed with borated pool water. The base case with boron had a concentration of 2000 ppm of boron in water. All cases studied here have no water in the guide tube locations, more closely representing the situation in an actual measurement.

### 5.1 Comparison of Borated Cases with the No- Borated Base Case

The base case with no boron and no water in the guide tube is compared with 1000 ppm, 1500 ppm, and 2000 ppm borated cases. In addition the C15 case with 2000 ppm of boron was also examined. As expected, the presence of boron makes the signal more sensitive to the local burnup as the thermal neutron signal becomes more localized. Table 6 and Figure 5 present these results with the mean, median, and standard deviation of the four data points at each detector.

**Table 6. Comparison of the Signal at various Boron Concentrations**

| Detector | G23-2000 ppm | C15-2000 ppm | G23-1000ppm | G23-1500ppm | Mean | Standard Deviation | Median |
|---|---|---|---|---|---|---|---|
| c | 0.767 | 0.855 | 0.818 | 0.794 | 0.809 | 0.038 | 0.806 |
| d | 0.824 | 0.899 | 0.859 | 0.844 | 0.857 | 0.032 | 0.852 |
| a | 0.874 | 1.000 | 0.905 | 0.891 | 0.917 | 0.056 | 0.898 |
| b | 0.801 | 0.881 | 0.843 | 0.824 | 0.837 | 0.034 | 0.833 |
| j | 0.792 | 0.843 | 0.836 | 0.812 | 0.821 | 0.023 | 0.824 |
| i | 0.810 | 0.896 | 0.850 | 0.830 | 0.846 | 0.037 | 0.840 |
| m | 0.933 | 0.966 | 0.949 | 0.944 | 0.948 | 0.014 | 0.947 |
| n | 0.853 | 0.858 | 0.889 | 0.870 | 0.868 | 0.016 | 0.864 |
| f | 0.829 | 0.828 | 0.871 | 0.851 | 0.845 | 0.021 | 0.840 |
| h | 0.872 | 0.867 | 0.893 | 0.885 | 0.879 | 0.012 | 0.879 |
| g | 0.965 | 0.983 | 0.973 | 0.969 | 0.973 | 0.008 | 0.971 |
| e | 0.848 | 0.884 | 0.882 | 0.866 | 0.870 | 0.017 | 0.874 |
| l | 0.831 | 0.834 | 0.870 | 0.852 | 0.847 | 0.018 | 0.843 |
| o | 0.867 | 0.855 | 0.887 | 0.880 | 0.872 | 0.014 | 0.873 |
| p | 1.000 | 0.945 | 1.000 | 1.000 | 0.986 | 0.027 | 1.000 |
| k | 0.885 | 0.841 | 0.901 | 0.894 | 0.880 | 0.027 | 0.889 |

A few observations can be made based on the results in Table 6. The signature resembles the non-borated case but tends to tilt downward in the region of high burn up. This can be noticed in the G23-2000 ppm and C15-2000 ppm. The corner with the high burn up is the “a, b, c, d” cluster (blue curve) of locations for the former and the “p, o, k, l” cluster for the latter (magenta curve) (see figure 1 for detector locations). The tilt is far less in the C15 case since the variation in the burnup is less severe in this case than in the base case, varying between 27 and 36 MWd/kg. The tilt in the curves becomes less severe for lower boron concentrations as can be seen in the 1000 and 1500 ppm cases for G23. This is as expected and is caused by the burnup having a more pronounced effect on the thermal signals.

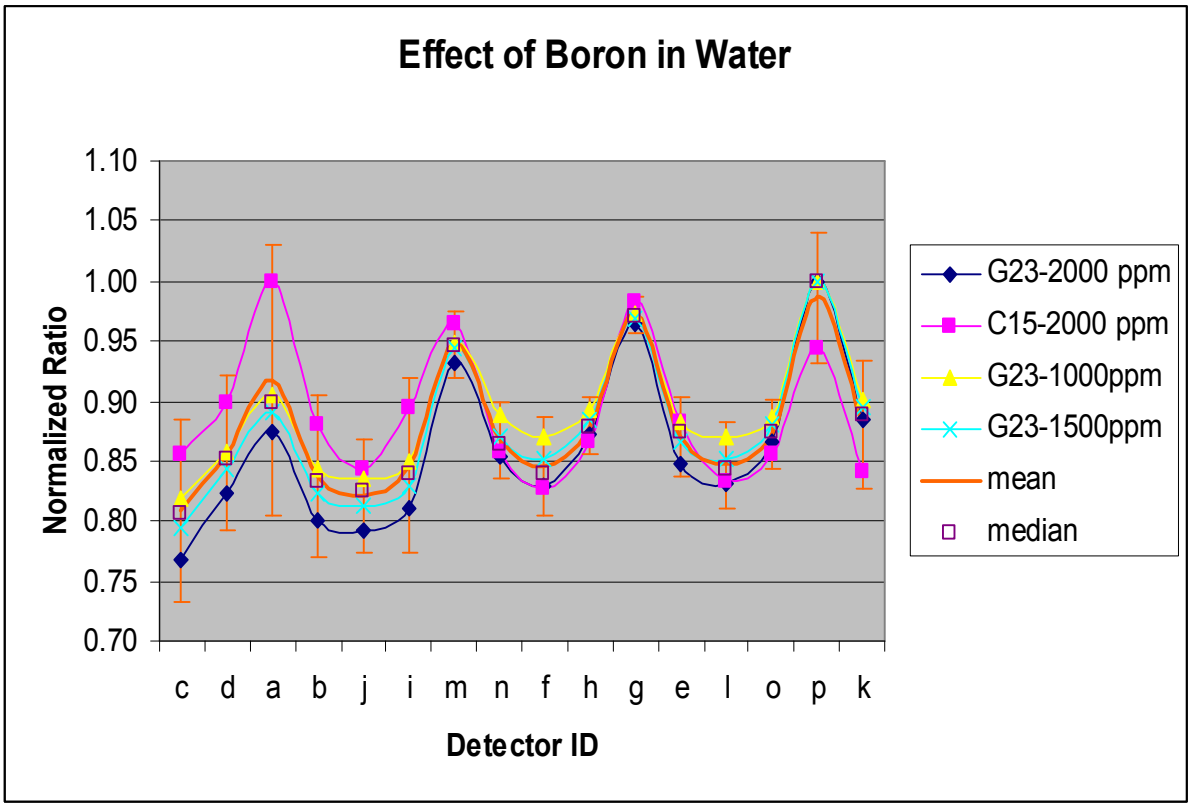


**Figure 5. Signal at Various Boron Concentrations (2-σ error bars shown)**

### 5.2 Borated Cases with Uniform Burnup and Very High Non-Uniform Burnup

Two cases with uniform burnups of 25 and 37 MWd/kg burnup and 2000 ppm of boron were added to the set of simulations. Two more cases where the highest burnup was 60 MWd/kg were studies. In one of these cases the burnup gradient varied from 30-60 MWd/kg, more severe than the G23 base case. The other case had a less severe gradient from 45-60 MWd/kg. Since all of these cases were run with 2000 ppm of boron, they are compared with the base G23 case with 2000 ppm boron in Table 7 and Figure 6.

The two uniform burnup cases exhibit the expected pattern of no tilt and resemble the non-borated case. The most extreme tilt is for the case with the extreme burnup (30-60 MWd/kg). Thus at the detector location "a" with the highest burnup, the standard deviation is 0.07.

**Table 7. Borated Cases with Varying Burnups**

| Detector | G23 | HiBU: 30-60 MWd/kg | HiBU: 45-60 MWd/kg | 24.9 MWd/kg | 37.3 MWd/kg | Mean | Std. Dev | Median |
|---|---|---|---|---|---|---|---|---|
| c | 0.767 | 0.795 | 0.771 | 0.818 | 0.849 | 0.800 | 0.034 | 0.795 |
| d | 0.824 | 0.812 | 0.794 | 0.883 | 0.894 | 0.841 | 0.045 | 0.824 |
| a | 0.874 | 0.887 | 0.837 | 0.999 | 0.992 | 0.918 | 0.073 | 0.887 |
| b | 0.801 | 0.813 | 0.777 | 0.881 | 0.890 | 0.832 | 0.050 | 0.813 |
| j | 0.792 | 0.825 | 0.814 | 0.822 | 0.855 | 0.822 | 0.023 | 0.822 |
| i | 0.810 | 0.821 | 0.812 | 0.880 | 0.896 | 0.844 | 0.041 | 0.821 |
| m | 0.933 | 0.919 | 0.909 | 0.998 | 1.000 | 0.952 | 0.044 | 0.933 |
| n | 0.853 | 0.862 | 0.866 | 0.881 | 0.894 | 0.871 | 0.016 | 0.866 |
| f | 0.829 | 0.815 | 0.824 | 0.819 | 0.843 | 0.826 | 0.011 | 0.824 |
| h | 0.872 | 0.888 | 0.864 | 0.883 | 0.888 | 0.879 | 0.011 | 0.883 |
| g | 0.965 | 0.961 | 0.933 | 1.000 | 0.999 | 0.972 | 0.028 | 0.965 |
| e | 0.848 | 0.852 | 0.839 | 0.882 | 0.885 | 0.861 | 0.021 | 0.852 |
| l | 0.831 | 0.858 | 0.802 | 0.816 | 0.847 | 0.831 | 0.023 | 0.831 |
| o | 0.867 | 0.872 | 0.840 | 0.881 | 0.893 | 0.870 | 0.020 | 0.872 |
| p | 1.000 | 1.000 | 1.000 | 0.996 | 0.994 | 0.998 | 0.003 | 1.000 |
| k | 0.885 | 0.894 | 0.865 | 0.878 | 0.895 | 0.883 | 0.012 | 0.885 |

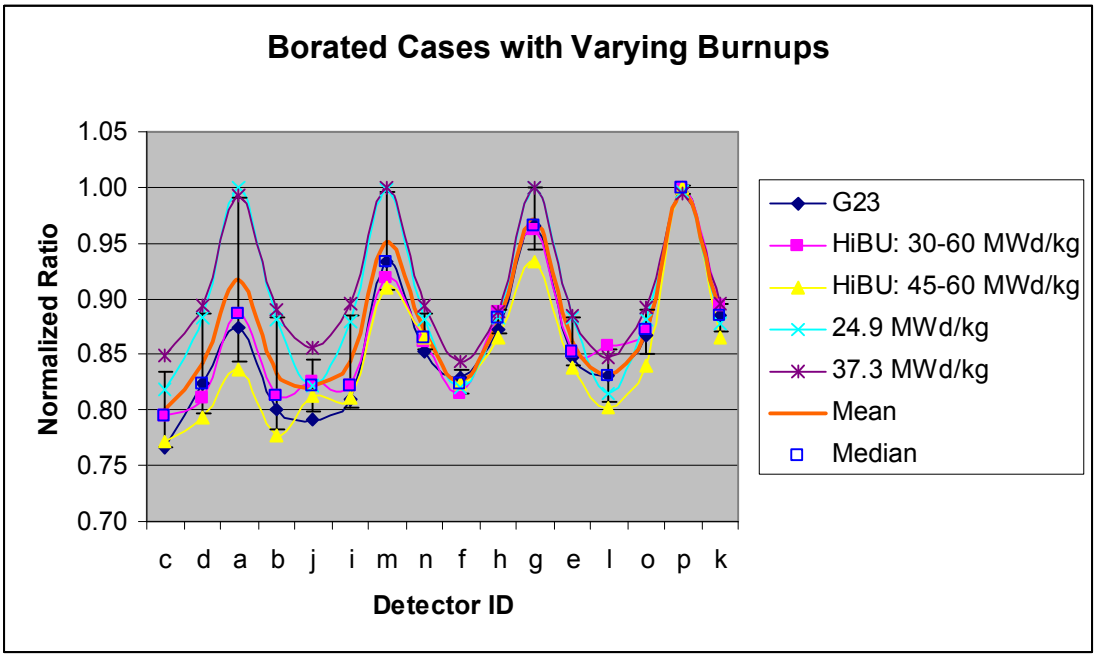


**Figure 6. Signal with Varying Burnups**

### 5.3 Sensitivity to Enrichment in the Borated Case

A final case with the G23 lattice with actual burnup profile but based on a 3% initial enrichment and 2000 ppm boron was examined. Results presented in Table 8 show that there is very little sensitivity to the enrichment variation as was the case without any boron (see Section 4.3)

**Table 8. Sensitivity to Enrichment in the Presence of Boron**

| Detector | G23 | G23-3% enriched |
|---|---|---|
| c | 0.767 | 0.766 |
| d | 0.824 | 0.82 |
| a | 0.874 | 0.87 |
| b | 0.801 | 0.806 |
| j | 0.792 | 0.798 |
| i | 0.81 | 0.814 |
| m | 0.933 | 0.926 |
| n | 0.853 | 0.852 |
| f | 0.829 | 0.832 |
| h | 0.872 | 0.872 |
| g | 0.965 | 0.952 |
| e | 0.848 | 0.849 |
| l | 0.831 | 0.835 |
| o | 0.867 | 0.866 |
| p | 1 | 1 |
| k | 0.885 | 0.88 |

### 5.4 Summary of the Borated Cases

A combined examination of the nine different cases studied with borated water discussed above in Section 5.1 through 5.3, can yield an overall mean signal and standard deviation at each detector location. Table 9 presents the mean, standard deviation and median values for the set. Figure 7 shows the signal with the standard deviation.

Examining the data from Table 9 and Figure 7, the distribution at each detector location from the nine runs, have the same mean and median. Thus, the ratio each detector location is fairly well behaved with a largest uncertainty of 0.063. It is noted that these cases selected were extreme ones with large burnup gradients that test the limits of variability of the signal at each location.

**Table 9. Mean Signal from all Borated Cases**

| Detector | Mean | Standard Deviation | Median |
|---|---|---|---|
| c | 0.804 | 0.034 | 0.795 |
| d | 0.848 | 0.038 | 0.844 |
| a | 0.917 | 0.063 | 0.891 |

| Detector | Mean | Standard Deviation | Median |
|---|---|---|---|
| b | 0.835 | 0.041 | 0.824 |
| j | 0.822 | 0.021 | 0.822 |
| i | 0.845 | 0.036 | 0.830 |
| m | 0.949 | 0.033 | 0.944 |
| n | 0.870 | 0.015 | 0.866 |
| f | 0.835 | 0.018 | 0.829 |
| h | 0.879 | 0.011 | 0.883 |
| g | 0.971 | 0.022 | 0.969 |
| e | 0.865 | 0.018 | 0.866 |
| l | 0.838 | 0.021 | 0.835 |
| o | 0.871 | 0.016 | 0.872 |
| p | 0.993 | 0.018 | 1.000 |
| k | 0.881 | 0.019 | 0.885 |

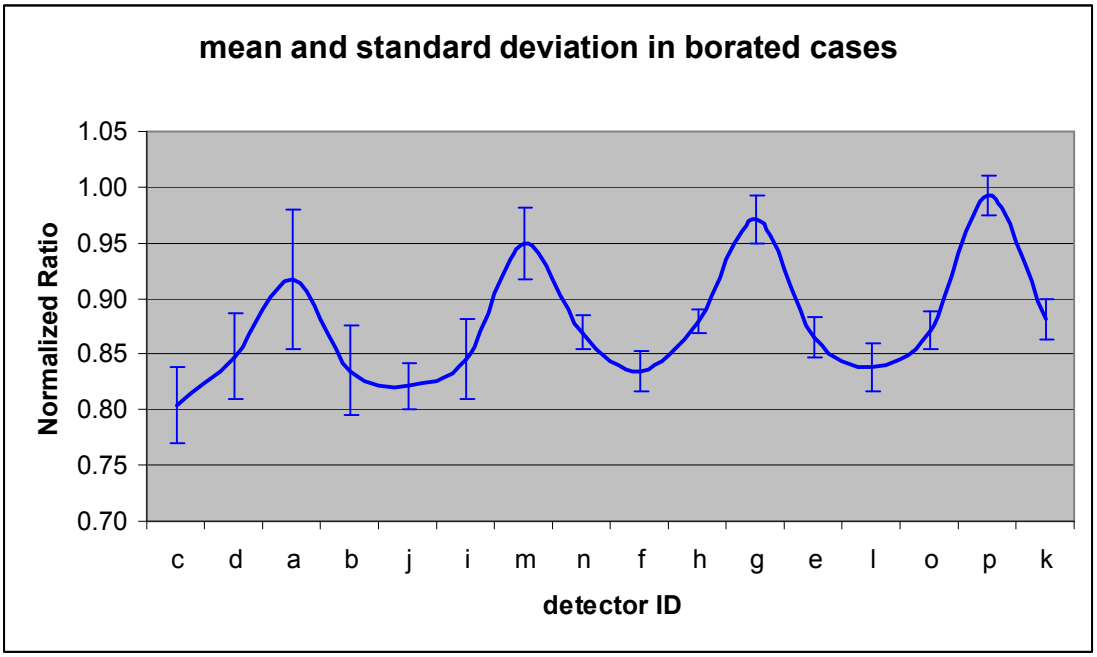


**Figure 7. Mean and Standard Deviation from the Borated Cases**

The highest standard deviation is at detector location "a". The other three locations (b, c, and d) also have higher standard deviations than typically the rest of the locations. This is because of the fact that in the non-uniform burnup cases, the high burnup pins are in the vicinity of these locations. It can be argued that this phenomenon can occur anywhere in the lattice. It is highly unlikely that a lattice will have completely randomly distributed burnups; typically the burnup will vary gradually from one general quadrant in the lattice to the next. Thus, it would be useful to cluster the sixteen detectors into three groups: the corner locations consisting of "a", "g", "p", and "m"; the central locations consisting of "c", "f", "l", and "j"; the remaining eight locations form the third group. The first group would be the one with the highest signal and any one of the four locations can potentially be the highest among them, i.e. with the normalized ratio equal to

1. Given this situation, it is useful to look at mean values and standard deviations for each of the three groups of detector locations.

The mean value for the corner group from the nine different runs is 0.957 with a standard deviation of 0.046. The mean value for the center group is 0.825 with a standard deviation of 0.027. The mean value for the remaining set of 8 detector locations is 0.862 with a standard deviation of 0.030. The total uncertainty of this set was derived by taking the square root of the sum of squares of the maximum uncertainty of the various parametric studies. The rounded up value for this was approximately 0.08. In addition, the constraint that the highest value of the corner group cannot exceed 1, the mean for this group can be lowered by 0.08 to a value of 0.92 , such that the upper limit will be 1. The remainder of the groups will have their true means. As a result of this a signal shape with an upper and lower bound can be constructed. Table 10 presents the generic signal with the upper and lower bounds that can be constructed from this data.

**Table 10. Generic Signal**

| Detector | Mean | Upper Bound | Lower Bound |
|---|---|---|---|
| c | 0.825 | 0.905 | 0.745 |
| d | 0.862 | 0.942 | 0.782 |
| a | 0.920 | 1.000 | 0.840 |
| b | 0.862 | 0.942 | 0.782 |
| j | 0.825 | 0.905 | 0.745 |
| i | 0.862 | 0.942 | 0.782 |
| m | 0.920 | 1.000 | 0.840 |
| n | 0.862 | 0.942 | 0.782 |
| f | 0.825 | 0.905 | 0.745 |
| h | 0.862 | 0.942 | 0.782 |
| g | 0.920 | 1.000 | 0.840 |
| e | 0.862 | 0.942 | 0.782 |
| l | 0.825 | 0.905 | 0.745 |
| o | 0.862 | 0.942 | 0.782 |
| p | 0.920 | 1.000 | 0.840 |
| k | 0.862 | 0.942 | 0.782 |

This generic signal with the upper and lower bounds for the most part captures the range of ratios in each of the three groups from the nine simulations it is based on. Figure 8 represents the final signal with upper and lower bounds.

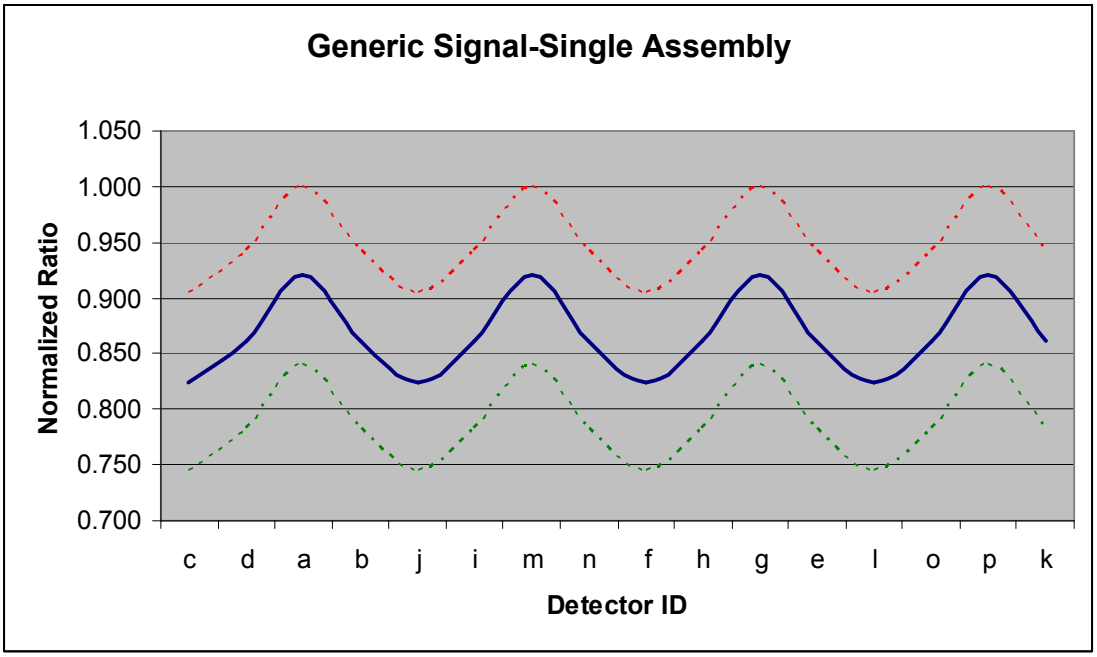


**Figure 8. Generic Signal**

It is emphasized that these bounds in Figure 8 represent typical variations at each location and that the shape of the signature is invariant with the peaks at the corners and the dips at the inner guide tube locations.

Perturbations from this generic shape can indicate missing fuel in an assembly. A few examples of missing pins and the consequent change in the signal shape are examined in the next section.

## 6.0 MISSING PIN CASES

Four different scenarios of missing pins will be examined in this section. The percentage of missing pins ranges from 4% to 12%. It must be noted that current methods can at best detect 50% or higher missing pins. They also rely on operator declared data to make these determinations. This methodology does not rely on any operator declared data to detect missing pins.

In the following examples the missing pins were replaced by stainless steel pins that would keep the mass of the assembly approximately the same as that of an intact assembly. Bubble diagrams show the location of the missing pins in red and also the percent deviation of the signal from the base case with no missing pins. These percent deviation numbers are meant to illustrate the sensitivity of the methodology to missing pins. The key indicator of missing pins will be the deviation of the signal shape from the generic signal shown in Figure 8. A combination of the deviation in shape as well as, to a lesser extent, ratios that lie outside the bounds of the generic expected values at a detector location will be indicators of missing fuel.

The following examples are intended to determine minimum fraction of missing pins that can be detected by this methodology.

### 6.1 Eight Missing Pins

Two scenarios with 8 missing pins, representing about 4% of the total 179 active pins, were studied. The missing pins were in a cluster of eight: in the first case in the high burnup region of the G23 lattice and the second in the low burnup region of the G23 lattice. Figures 9 and 10 show the locations of the missing pins in red.

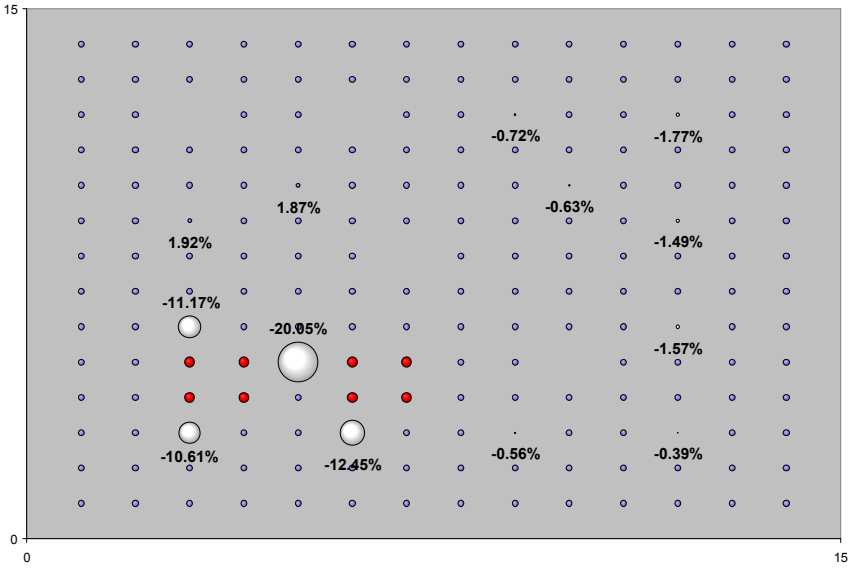


**Figure 9. Eight Pins Missing: High Burnup Region**

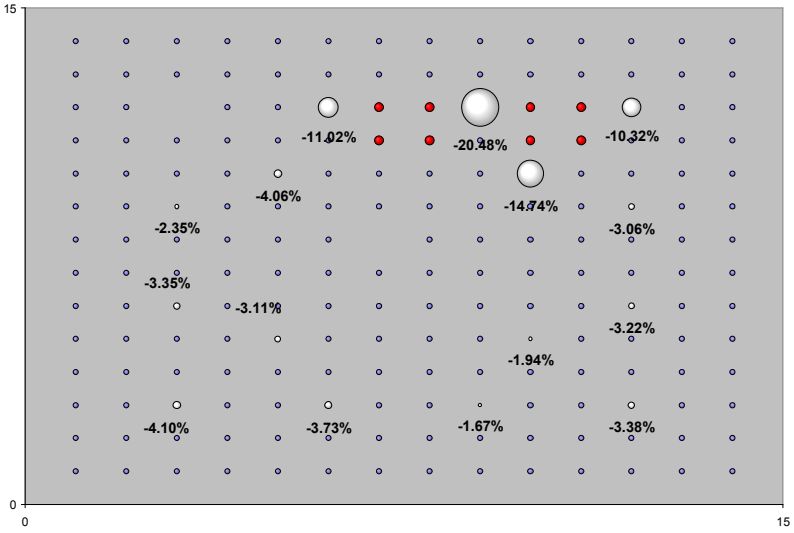


**Figure 10. Eight Missing Pins: Low Burnup Region**

The two figures above show the large sensitivity of >10% in the vicinity of the missing pins. Figures 11 and 12 illustrate the impact on the signal shape as a result of the missing pins.

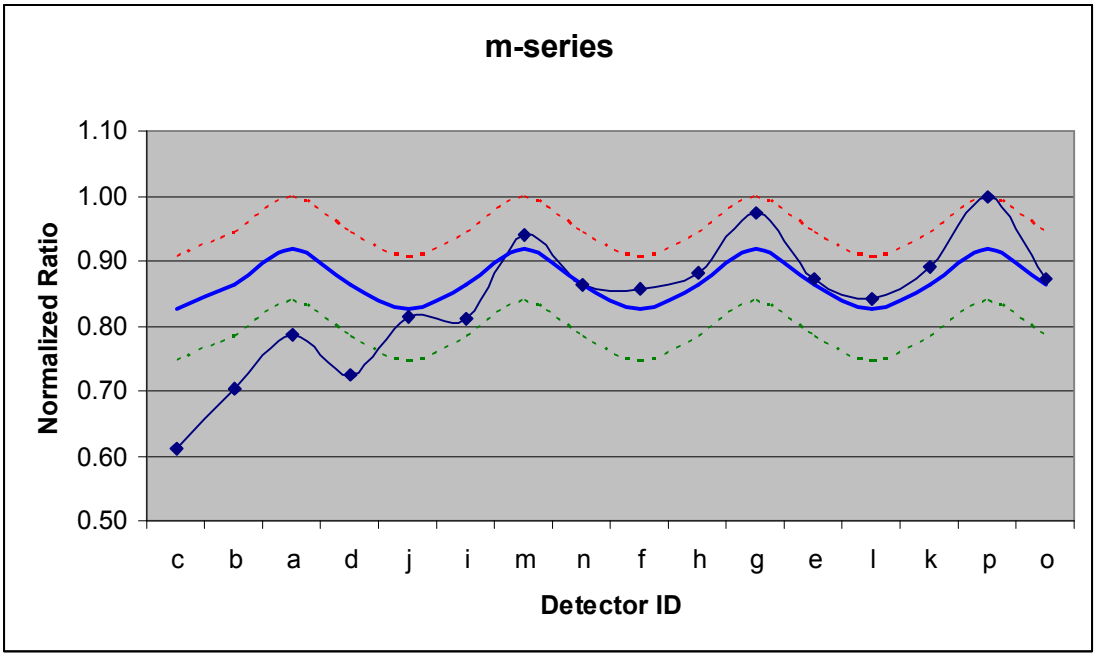


**Figure 11. Signal from Eight Missing Pins: High Burnup Region**

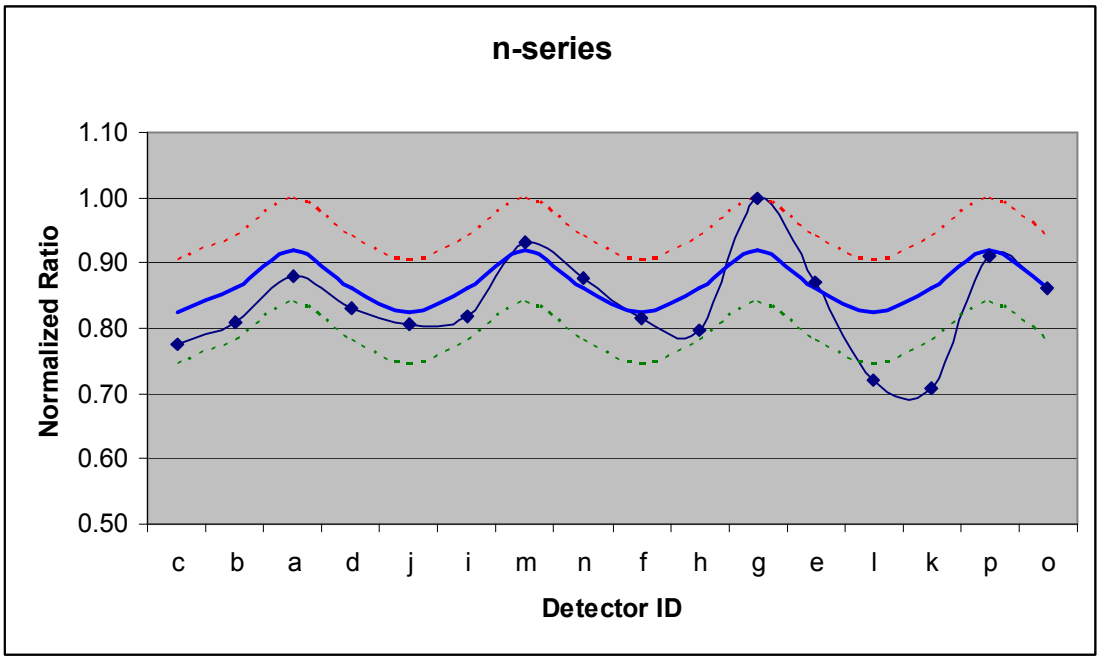


**Figure 12. Signal from Eight Missing Pins: Low Burnup Region**

Figure 11 shows a small deviation from the expected shape coupled with a more than expected drop in the ratio in the vicinity of the missing pins. Figure 12 shows no discernable deviation in shape though there is a more than expected drop in the ratio in the vicinity of the missing pins. These two cases represent situations where the 4% of missing pins are in clusters and show borderline detectability.

### 6.2 Random Distribution of Missing Pins

This case represents a scenario where 10 pins are missing in a random manner with no clustering of missing pins. This represents a 6% fraction of the total number of pins. Figure 13 and 14 represent this case.

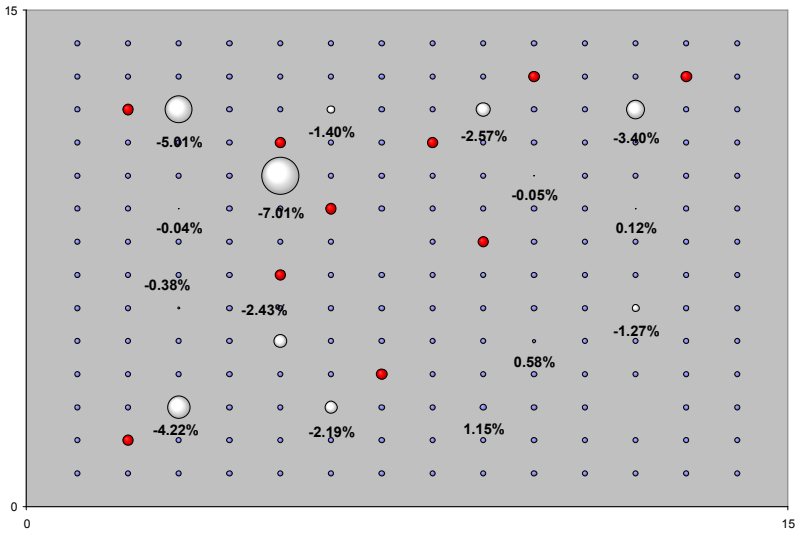


**Figure 13. Ten Pins Missing**

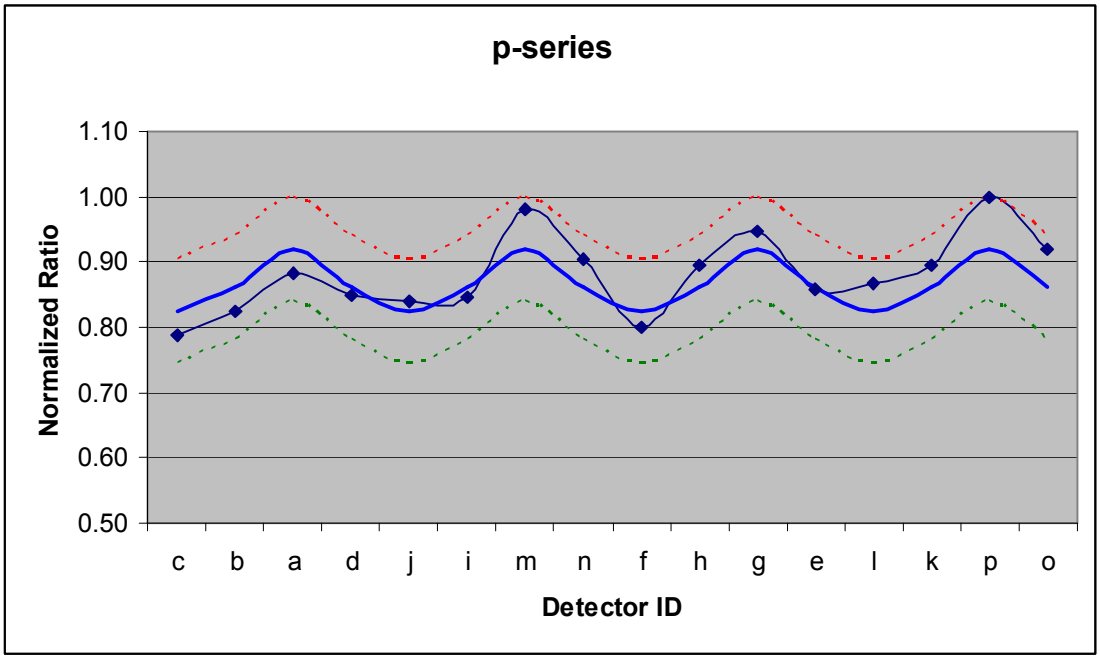


**Figure 14. Signal from Ten Missing Pins**

This case also shows that diversion of 6% of the pins in a dispersed manner is difficult to detect since neither the shape or change in ratio is sufficient to determine diversion.

### 6.3 Twenty Two Missing Pins

This case represents a scenario of approximately 12% of missing pins with a large number of these clustered together. This case was run with the C15 lattice since this is a test assembly at KAERI with this pattern of missing fuel. Figures 15 and 16 show the results. Further discussion of this case will be presented in the section on benchmarking the computer simulation.

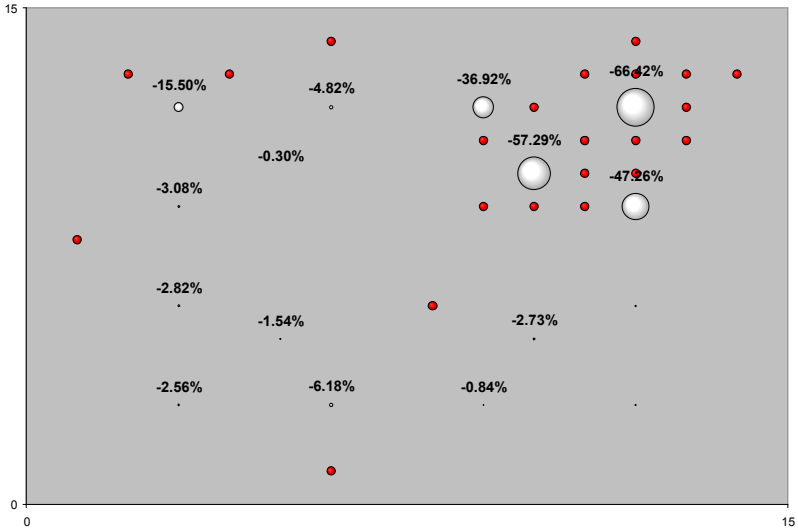


**Figure 15. Twenty Two Missing Pins**

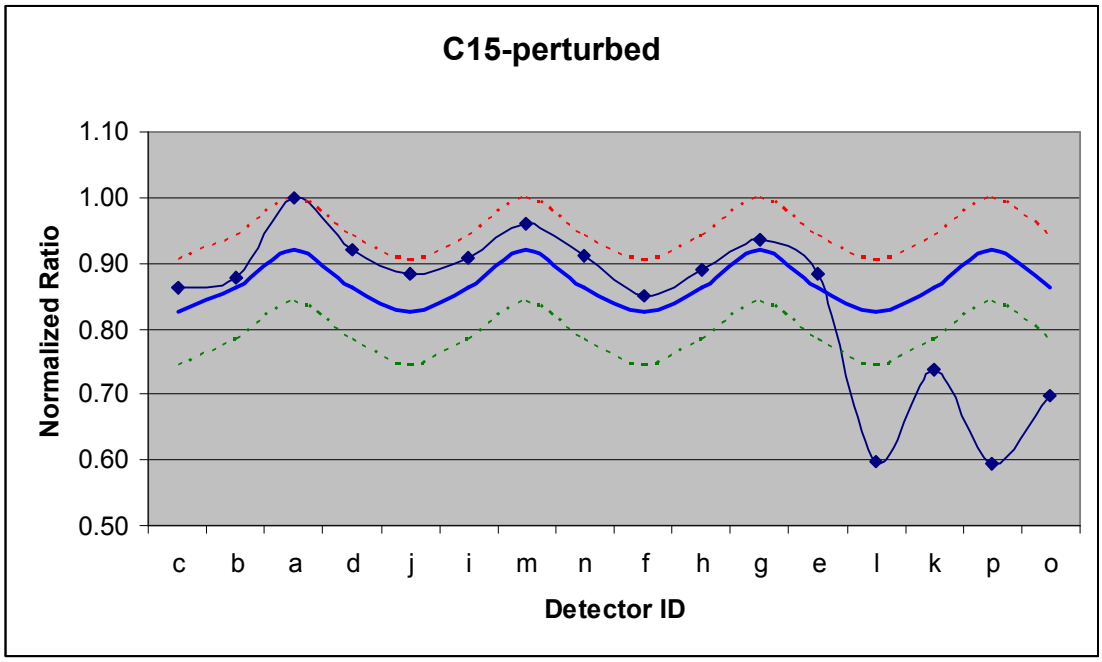


**Figure 16. Signal from the Twenty Two Missing Pin Case**

This case shows a clear deviation from the base signature that is readily apparent with both a change in the shape as well as a precipitous drop in the ratio in the region where several pins are missing.

### 6.4 Summary of Missing Pin Cases- Single Assembly

The set of simulations shown in the previous sub-sections indicate that the threshold of detection of diversion is about 10% missing pins from the assembly, though in some cases of smaller fractions of missing pins being clustered, detection could be possible. In more realistic scenarios, it is likely that much larger number of fuel pins will be removed from an assembly, and this methodology shows the potential to detect these diversions without any input from the operator. Current methods rely on operator declared data and cannot reliably detect diversions of less than 50% on missing pins. Thus, this methodology promises to be a powerful tool in detecting even small fractions of missing fuel from a spent fuel assembly [9,10,11].

## 7.0 OTHER PWR FUEL TYPES

Signatures similar to the 14 x 14 fuel type can be developed for other PWR fuel product lines. One of the more common fuels used nowadays is the 17 x 17 type. A few preliminary studies were performed with a fuel lattice from the Takahama reactor [12]. Since the actual burnup map for the pins in the lattice was unknown, a uniform burnup of 35.4 MWd/kg was used for the non-Gd pins. The fourteen pins with Gd in them were modeled as having a burnup of 28.2 MWd/kg. As in the case of the Kori1 fuel, a 10-year cooling time was used to obtain the source and isotopics. A case was also run with a uniform burnup of 35.4 MWd/kg in all pins.

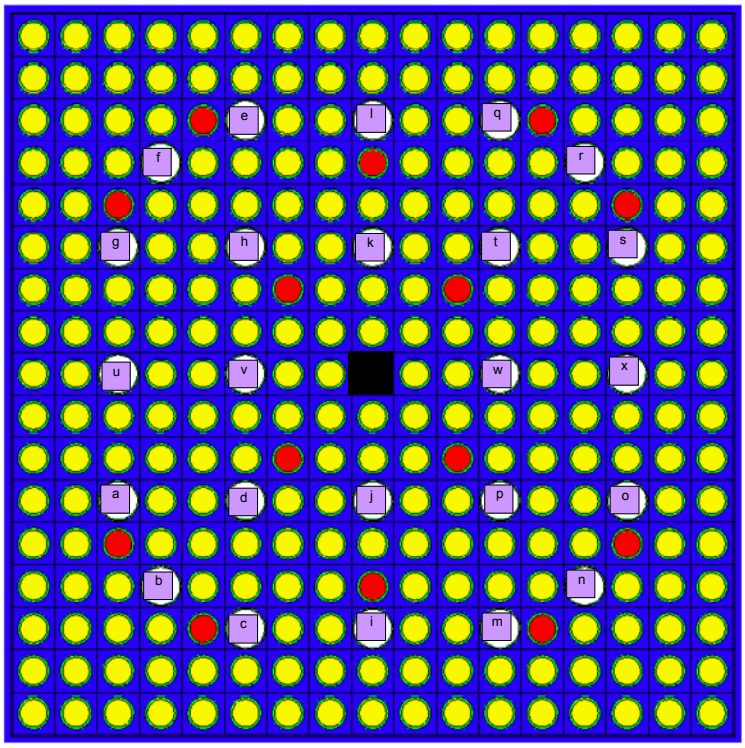


**Figure 17. Takahama 17 x 17 Fuel**

Figure 17 shows the layout of the fuel with the 24 guide tube locations (marked a through x). The red fuel pins contain Gd as burnable poison. The perturbed case had six pins missing (marked "M") as shown in Figure 18. The six missing pins represent about 2% of the total active pins in the lattice.

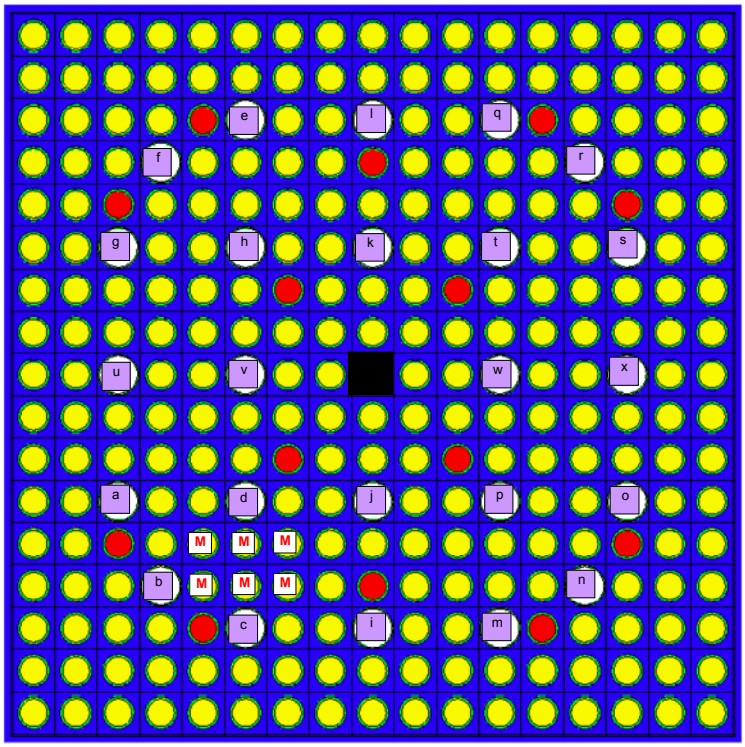


**Figure 18. Missing Pins in Perturbed Case**

Table 11 presents the normalized ratios for the 24 detector locations for the base cases (one and two burnup). Figure 19 shows the base signal from these two cases as well as the perturbed signal. From the figure it is clear that a unique signature can be established for the 17 x 17 fuel in a manner similar to the 14 x 14 fuel. Once again the data for the corner clusters of four detectors is plotted in a counter clockwise manner starting with the inner location followed by the two detectors in the arm of the cruciform pattern that continue in a counter clockwise manner (e.g. d,a,b,c,i,j etc.). The order in which the detectors are listed in Table 11 will produce the unique signature found in Figure 19. As before, other patterns can be formed for the base signal, but following the prescribed order will produce this unique signature.

The perturbed case shows a clear deviation from the normal and further validates the methodology.

Further studies on the 17 x 17 fuel type as well as other fuel product lines need to be undertaken to complete the set of unique signatures that can be established for the various PWR fuel product lines.

**Table 11. Takahama 17 x 17 Base Case Ratios**

| Detector | Two Burnup Case | One Burnup Case |
|---|---|---|
| d | 0.882 | 0.869 |
| a | 0.935 | 0.941 |
| b | 0.986 | 0.998 |
| c | 0.943 | 0.944 |
| i | 0.904 | 0.892 |
| j | 0.832 | 0.818 |
| h | 0.872 | 0.874 |
| e | 0.937 | 0.935 |
| f | 0.995 | 0.992 |
| g | 0.932 | 0.937 |
| u | 0.921 | 0.898 |
| v | 0.836 | 0.815 |
| p | 0.873 | 0.869 |
| m | 0.934 | 0.935 |
| n | 1.000 | 0.992 |
| o | 0.937 | 0.944 |
| x | 0.912 | 0.894 |
| w | 0.832 | 0.816 |
| t | 0.877 | 0.873 |
| s | 0.944 | 0.939 |
| r | 0.992 | 1.000 |
| q | 0.929 | 0.936 |
| l | 0.895 | 0.895 |
| k | 0.824 | 0.817 |

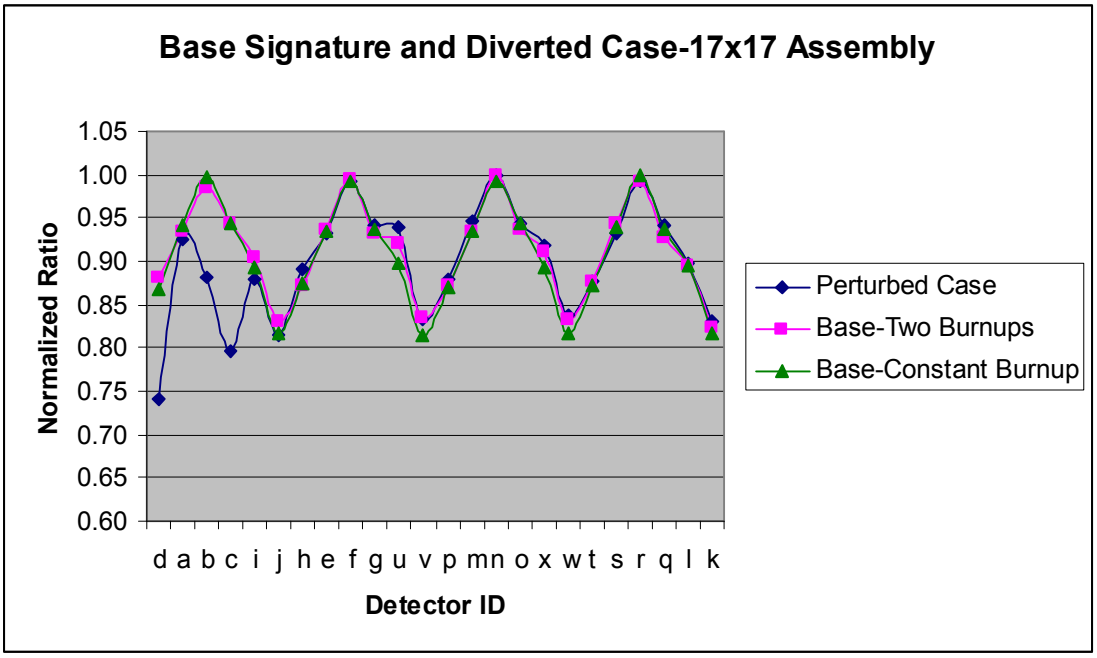


**Figure 19. Signature from 17 x17 Takahama Lattice**

## 8.0 IN-SITU STUDIES

The previous sections demonstrated that a unique signature can be developed for various intact PWR spent fuel assemblies that were isolated in the spent fuel pool. This signature is visibly perturbed when fuel pins are missing or are replaced by stainless steel pins. However, the ability to detect partial defects without moving an assembly is important since this would present a minimally intrusive condition. Typically, reactor operators are unwilling to move assemblies out of their storage positions, an operation that would be necessary if the assembly needs to be isolated to perform the measurements. Unnecessary movement of assemblies also increases the potential of having a fuel handling accident [13]. Thus, while this promises to be a powerful methodology to detect partial defects, the technique will more readily lend itself to the development of a practical tool if it works with the assembly in an in-situ condition, i.e. with the assembly in the storage rack surrounded by other assemblies [13].

This section will examine the sensitivity of the signature to various conditions while the assembly is in an in-situ condition.

### 8.1 Model for In-Situ Simulation

The same lattice used as the base model for the isolated assembly case was used to perform these studies. The model consisted of a 3 x 3 array consisting of this lattice with the assembly in the center representing the test assembly where measurements would be made. Since the condition of the surrounding assemblies would impact the test assembly it would be impossible to model every possible combination of burnup and other parameters that exist. The approach taken was to randomly rotate all nine assemblies and examine the impact on the base signature in each case. It will be recalled that the chosen lattice has an extreme gradient in burnup, the parameter that has most impact on the signature. Thus, rotating these assemblies in a random manner would result in a variety of combinations of burnup orientations that the test assembly will experience. This would present conditions of differing in-leakage, particularly of neutrons, from the surrounding assemblies into the test assembly. Figure 20 shows one case with the nine assemblies in different orientations in relation to each other.

The nine assemblies are placed in a storage rack consisting of stainless steel frames with thin boral plates in between the assemblies. The water contains 2000 ppm of boron, which represents a typical concentration in spent fuel pools. Seventeen cases with different orientations were studied: 13 cases with the nine assemblies containing the base lattice oriented randomly (including one with all oriented the same way), a case with a single assembly with periodic boundary conditions on all sides, a case with uniform high burnup (~40 MWd/kg) pins in all nine assemblies, a case with the test assembly at uniform high burnup (~40 MWd/kg) surrounded by high (~40 MWd/kg) and low (~27 MWd/kg) assemblies, and a case with the test assembly at uniform low burnup (~27 MWd/kg) surrounded by high (~40 MWd/kg) and low (~27 MWd/kg) assemblies. The average normalized ratio of the gamma-to thermal neutron signals at each of the sixteen guide tube locations was determined from these 17 different cases. This data is presented in Table 12. In addition, Table 12 also contains data from a case with all 9 assemblies containing pins with a uniform burnup of 33 MWd/kg as well as the average of the single assembly with no boron (this is plotted separately in Figure 3).

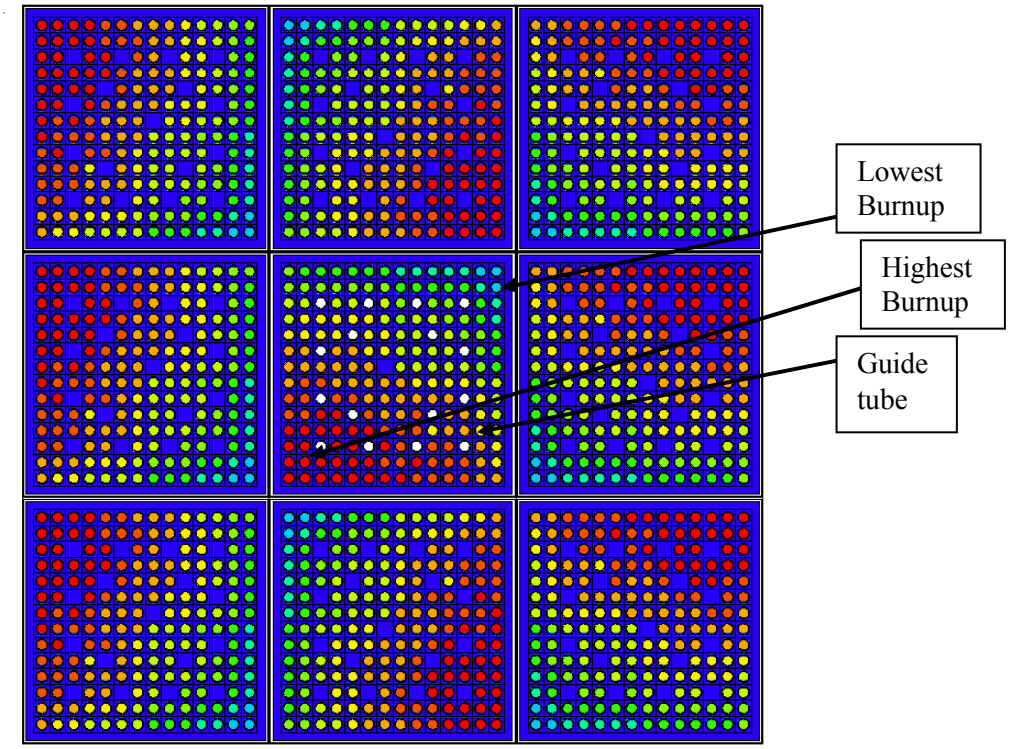


**Figure 20. 3x3 Spent Fuel Assemblies in Storage Rack**

**Table 12. Comparison of Varying and Uniform Burnup Multi-Assembly Ratios**

| Detector | Average of 17 Multi-Bundle Cases | Standard Deviation of 17 cases | Uniform Multi-Bundle Case | Average of Single Bundle Cases with no Boron |
|---|---|---|---|---|
| c | 0.860 | 0.014 | 0.866 | 0.913 |
| d | 0.910 | 0.014 | 0.918 | 0.929 |
| a | 0.993 | 0.011 | 0.990 | 0.992 |
| b | 0.923 | 0.012 | 0.931 | 0.925 |
| j | 0.847 | 0.027 | 0.876 | 0.917 |
| i | 0.902 | 0.020 | 0.927 | 0.929 |
| m | 0.965 | 0.032 | 1.000 | 0.996 |
| n | 0.887 | 0.036 | 0.905 | 0.929 |
| f | 0.841 | 0.027 | 0.878 | 0.908 |
| h | 0.856 | 0.045 | 0.918 | 0.930 |
| g | 0.925 | 0.042 | 0.991 | 0.993 |
| e | 0.887 | 0.022 | 0.921 | 0.931 |
| l | 0.815 | 0.047 | 0.869 | 0.915 |
| o | 0.839 | 0.056 | 0.914 | 0.930 |
| p | 0.874 | 0.075 | 0.977 | 0.997 |
| k | 0.837 | 0.050 | 0.930 | 0.928 |

Fission neutrons migrate and slow down to thermal energies resulting in a less localized signal that is caused by particles from more than just neighboring pins. In an isolated assembly, the

corner locations see less of a thermal neutron signal than do the interior locations since these have contributions from fewer pins than do the interior locations. However, when assemblies are surrounded by other assemblies, there will also be neutrons migrating between assemblies. The net leakage will be towards regions with lower neutron populations such as the low burnup regions. The fission neutrons are only minimally impacted by the presence of boron in the system. Once thermalized, they contribute to the neutron signal in the local guide tube locations. While there is some contribution to the gamma signal from neighboring assemblies this is minimal owing to the presence of the high-density, high-Z material in the form of fuel.

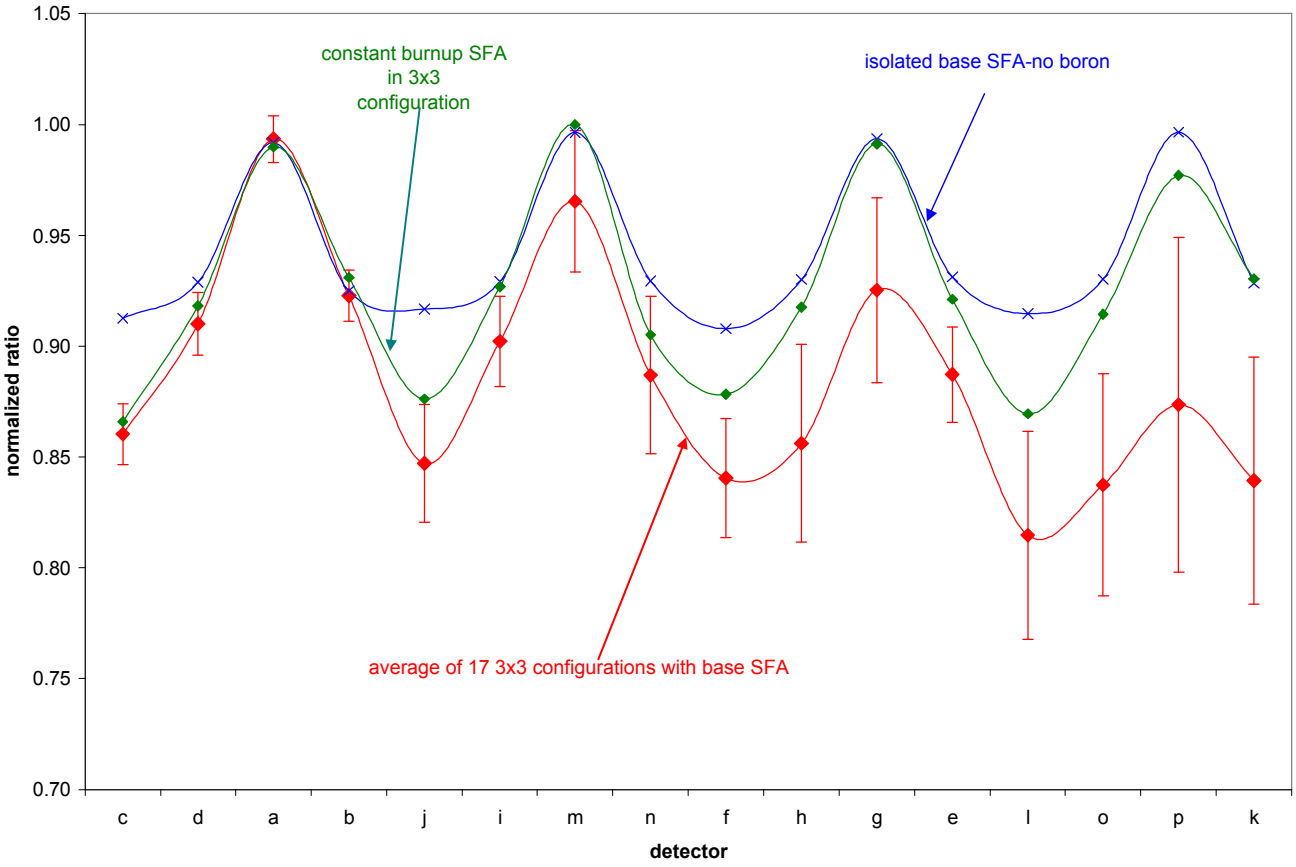


**Figure 21. Signature from Seventeen Random Orientations of the 3x3 Configuration**

Therefore, while the gamma signal is less sensitive to the presence of neighboring assemblies, the thermal neutron signal increases, with this increase being greater in the lower burnup regions of an assembly. This accounts for the tilt of the average signature for the 17 varying burnup configurations seen in Figure 21. It is also noted that the uncertainty in the low burnup region is greater since the random rotations can place high as well as low burnup pins in the neighborhood of the low burnup part of the central assembly. Figure 21 also presents the signature from a case where all nine assemblies have constant burnups as well as the signature from the base assembly isolated with no dissolved boron. When all assemblies have the same burnup the net migration from neighboring assemblies is minimal and the tilt in the signature virtually disappears and is very close to the signature from an isolated assembly with no dissolved boron. Table 13 presents comparisons of the thermal neutron and gamma signals at the sixteen guide tube locations for

one of the randomly rotated configurations of the multi-assembly case with an isolated case, both cases having the same dissolved boron concentration of 2000 ppm.

**Table 13. Comparison of Thermal Neutron and Gamma Signals between a Multi-Assembly Case and an Isolated Assembly Case**

| Detector | Thermal Neutron Signal (neutrons/s) | | | Gamma Signal (gammas/s) | | |
|---|---|---|---|---|---|---|
| | Multi | Single | Ratio | Multi | Single | Ratio |
| c | 1.37E+06 | 5.69E+05 | 0.42 | 7.23E+12 | 7.06E+12 | 0.98 |
| d | 1.29E+06 | 5.15E+05 | 0.4 | 7.16E+12 | 6.87E+12 | 0.96 |
| a | 1.21E+06 | 4.86E+05 | 0.4 | 7.43E+12 | 6.88E+12 | 0.93 |
| b | 1.29E+06 | 5.46E+05 | 0.42 | 7.44E+12 | 7.08E+12 | 0.95 |
| j | 1.32E+06 | 5.10E+05 | 0.39 | 6.77E+12 | 6.54E+12 | 0.97 |
| i | 1.28E+06 | 5.15E+05 | 0.4 | 7.01E+12 | 6.76E+12 | 0.96 |
| m | 1.17E+06 | 4.08E+05 | 0.35 | 6.71E+12 | 6.16E+12 | 0.92 |
| n | 1.22E+06 | 4.32E+05 | 0.35 | 6.48E+12 | 5.97E+12 | 0.92 |
| f | 1.23E+06 | 4.63E+05 | 0.38 | 6.36E+12 | 6.21E+12 | 0.98 |
| h | 1.10E+06 | 3.81E+05 | 0.35 | 5.72E+12 | 5.39E+12 | 0.94 |
| g | 1.02E+06 | 3.37E+05 | 0.33 | 5.76E+12 | 5.27E+12 | 0.91 |
| e | 1.21E+06 | 4.58E+05 | 0.38 | 6.55E+12 | 6.29E+12 | 0.96 |
| l | 1.20E+06 | 4.14E+05 | 0.34 | 5.83E+12 | 5.57E+12 | 0.96 |
| o | 1.17E+06 | 3.80E+05 | 0.33 | 5.68E+12 | 5.33E+12 | 0.94 |
| p | 1.02E+06 | 2.85E+05 | 0.28 | 5.12E+12 | 4.62E+12 | 0.9 |
| k | 1.09E+06 | 3.56E+05 | 0.33 | 5.45E+12 | 5.10E+12 | 0.93 |

The data in Table 13 clearly illustrates the impact of surrounding assemblies on the test assembly. As discussed earlier, the gamma signal is within 10% of the isolated case while the neutron signal is heavily influenced by the surrounding assemblies. This is consistent with the tilt in the normalized ratio in the low burnup regions (e.g. detector location k, l, o, p etc) seen in Figure 21. It is emphasized again that the basic shape still remains the same as with a single assembly case and it is the deviation from the shape rather than the values of the individual ratios that will determine whether diversion has occurred. It is also noted from Table 13 that the standard deviation for the most part is within 0.05. There are two locations in the low burnup region where it exceeds 0.05. It must be noted that the model used here is an extreme one with a large burnup gradient within the test and surrounding assemblies. Consequently, this study presents the extreme conservative bounds of this variation. In reality, assemblies will not have such large burnup gradients and thus will have standard deviations within the 0.05 limit.

### 8.2 Effect of Boron Concentration

In addition to the effect of burnup, the boron concentration also has an impact on the signature. Four cases with different boron concentrations were examined. In addition to the base case of 2000 ppm dissolved boron, concentrations of 1500, 1000, and 0 ppm were studied. Table 14 and Figure 22 present the data from these studies.

**Table 14. Boron Sensitivity Studies**

| Detector | 2000 ppm | 1500ppm | 1000 ppm | 0 ppm |
|---|---|---|---|---|
| c | 0.859 | 0.864 | 0.854 | 0.835 |
| d | 0.901 | 0.910 | 0.905 | 0.885 |
| a | 1.000 | 1.000 | 1.000 | 1.000 |
| b | 0.932 | 0.937 | 0.923 | 0.913 |
| j | 0.832 | 0.829 | 0.825 | 0.805 |
| i | 0.892 | 0.891 | 0.882 | 0.865 |
| m | 0.928 | 0.930 | 0.930 | 0.909 |
| n | 0.860 | 0.855 | 0.840 | 0.825 |
| f | 0.838 | 0.831 | 0.816 | 0.782 |
| h | 0.841 | 0.835 | 0.821 | 0.776 |
| g | 0.919 | 0.914 | 0.894 | 0.861 |
| e | 0.879 | 0.871 | 0.868 | 0.843 |
| l | 0.785 | 0.778 | 0.771 | 0.736 |
| o | 0.790 | 0.790 | 0.774 | 0.750 |
| p | 0.811 | 0.809 | 0.792 | 0.767 |
| k | 0.815 | 0.812 | 0.790 | 0.751 |

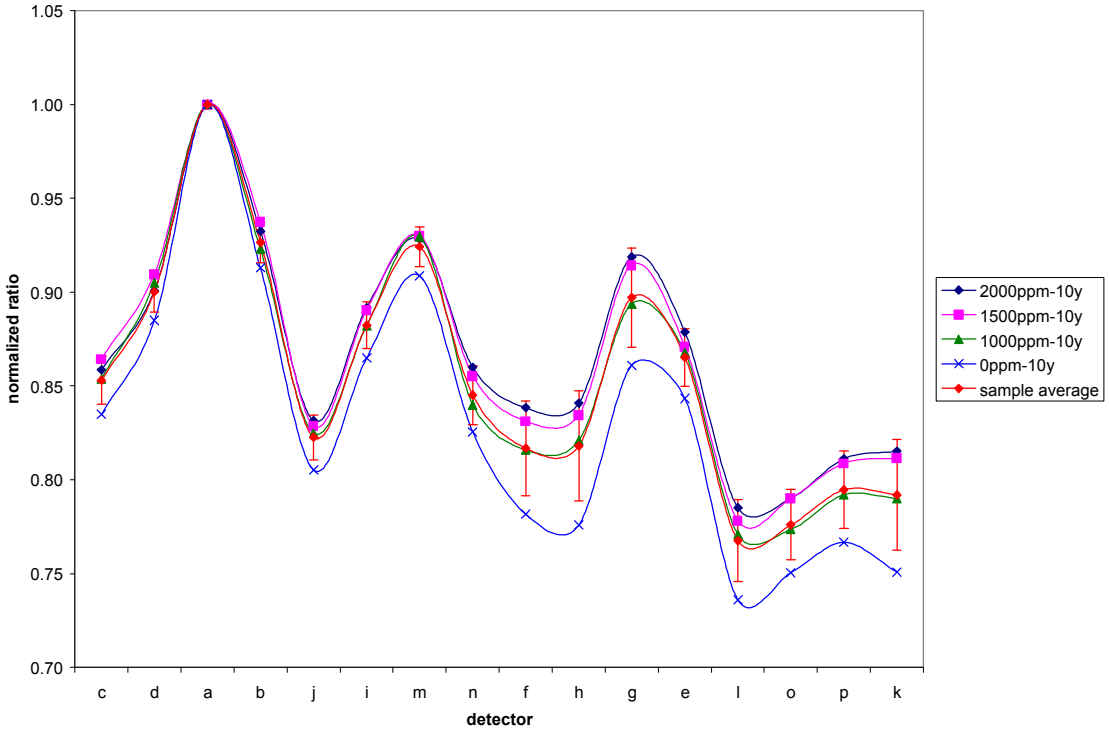


**Figure 22. Boron Sensitivity in a Multi-Assembly Configuration**

Comparing Figure 22 with Figure 5, which depicts the sensitivity to the boron concentration in an isolated assembly, the trends are reversed. In the case of the isolated assembly, the tilt is toward the high burnup region since the low burn up regions see fewer thermal neutrons than they would if the water did not contain any boron since there is an in-flow of thermal neutrons from the high burnup regions to the low burnup regions that is now smaller due to the localization effect of the boron. In the multi-assembly configuration used in this study, the low burnup region in the test assembly has high burnup regions adjacent to it. As a result, there is sufficient in-flow of neutrons that the tilt occurs toward that region. As the boron concentration decreases, the tilt grows more pronounced as more neutrons are able to flow into the low burnup regions relative to the flow into the high burnup regions.

### 8.3 Cooling Time Sensitivity

Studies were also repeated for the sensitivity of the signature for cooling time variation. The two cooling times studied were 10 and 20 years. Table 15 presents these results for the two cooling times at two different dissolved boron concentrations: 2000 ppm and 0 ppm.

**Table 15. Sensitivity to Cooling Times**

| Detector | 2000ppm-10y | 2000ppm-20y | 0ppm-10y | 0ppm-20y |
|---|---|---|---|---|
| c | 0.859 | 0.867 | 0.835 | 0.847 |
| d | 0.901 | 0.913 | 0.885 | 0.897 |
| a | 1.000 | 1.000 | 1.000 | 1.000 |
| b | 0.932 | 0.937 | 0.913 | 0.919 |
| j | 0.832 | 0.849 | 0.805 | 0.817 |
| i | 0.892 | 0.911 | 0.865 | 0.885 |
| m | 0.928 | 0.962 | 0.909 | 0.945 |
| n | 0.860 | 0.885 | 0.825 | 0.850 |
| f | 0.838 | 0.880 | 0.782 | 0.816 |
| h | 0.841 | 0.894 | 0.776 | 0.826 |
| g | 0.919 | 0.957 | 0.861 | 0.904 |
| e | 0.879 | 0.909 | 0.843 | 0.874 |
| l | 0.785 | 0.824 | 0.736 | 0.768 |
| o | 0.790 | 0.830 | 0.750 | 0.787 |
| p | 0.811 | 0.860 | 0.767 | 0.811 |
| k | 0.815 | 0.857 | 0.751 | 0.800 |

The variation in the signal is less 0.05 in all cases. Studies on initial enrichment were not separately performed for the multi-assembly case since the variation was shown to be minimal in the single assembly case. Based on the isolated assembly studies, the impact of enrichment was quite small (see Table 8) with a maximum difference of <0.02.

### 8.4 Conclusions from Multi-Assembly Studies

A base signature can therefore be established that retains a shape that is principally influenced by the location of the guide tube in the SFA. As explained earlier, the corner locations which are less influenced by surrounding fuel pins form the peaks of this signature while the central locations form the low points, i.e., the neutron and gamma signals are higher at the central locations. The central to corner guide tube gamma signal ratio is larger than that of the thermal neutrons. The other locations make up the rest of the shape transitioning from the peak to the valley in the signature. The presence of surrounding SFAs in an in-situ condition tilts the signature downward in the low burnup regions because of the relatively higher neutron migration from these SFAs to these regions compared with the migration to the high burnup regions. The amount of downward tilt towards regions of lower burnup will vary depending on the burnup in the regions of the neighboring SFAs that border these regions. The base case SFA examined here has a large burnup gradient; more uniform burnup cases tend to make the signature more symmetric. Gamma signals are almost entirely local and little leakage occurs from adjacent assemblies.

It must be borne in mind that this signature can be such that any of the locations a, g, m, or p can have the highest relative ratio of 1 and the location c, f, j or l can have the lowest relative ratio. Thus, it would be useful to construct bounding shapes based on averages of each of these sets as well as the remaining eight guide tube locations and applying uncertainties on them. The constraint on this will be that the corner locations can have a maximum value of 1. The uncertainty has been calculated as the square root of the sum of squares of the maximum uncertainty from each of the sensitivity studies described above. This value was rounded up to 0.1. Applying this uncertainty of ±0.1, a maximum and minimum bound of the average base signature has been constructed. Deviation, primarily of shape and secondarily of magnitude beyond these bounds, would indicate missing fuel from a SFA. Figure 23 and Table 16 present this data showing the maximum and minimum bounds of the signature.

**Table 16. Base Signature data**

| Detector | Mean | Upper Bound | Lower Bound |
|---|---|---|---|
| c | 0.8268 | 0.9268 | 0.7268 |
| d | 0.8646 | 0.9646 | 0.7646 |
| a | 0.9000 | 1.0000 | 0.8000 |
| b | 0.8646 | 0.9646 | 0.7646 |
| j | 0.8268 | 0.9268 | 0.7268 |
| i | 0.8646 | 0.9646 | 0.7646 |
| m | 0.9000 | 1.0000 | 0.8000 |
| n | 0.8646 | 0.9646 | 0.7646 |
| f | 0.8268 | 0.9268 | 0.7268 |
| h | 0.8646 | 0.9646 | 0.7646 |
| g | 0.9000 | 1.0000 | 0.8000 |
| e | 0.8646 | 0.9646 | 0.7646 |
| l | 0.8268 | 0.9268 | 0.7268 |
| o | 0.8646 | 0.9646 | 0.7646 |
| p | 0.9000 | 1.0000 | 0.8000 |
| k | 0.8646 | 0.9646 | 0.7646 |

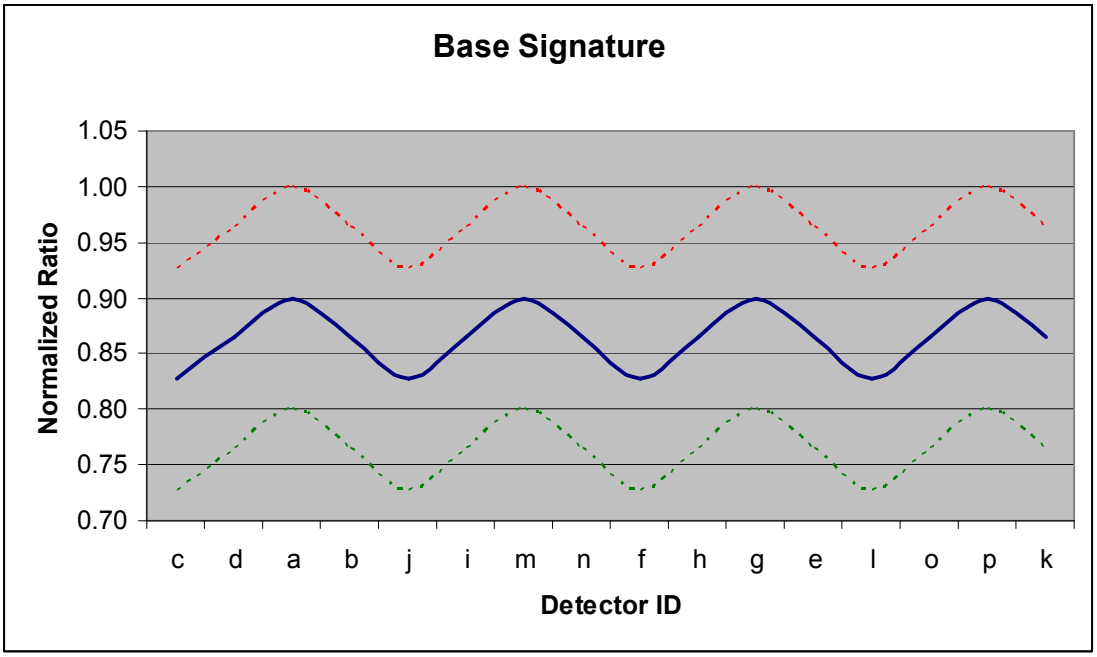


**Figure 23. Base Signature showing Upper and Lower Bounds**

The important point that can be inferred from these extensive studies involving both isolated and multi-bundle cases is that a basic shape that is principally dependent on the geometric lay out of the guide tubes in a particular type of fuel assembly. Thus perturbation of the assembly by fuel pin removal will change the shape of this signature enabling detection of the defect. The next section will examine the impact of removing approximately 12% of the pins from the base assembly.

## 9.0 PIN DIVERSION CASES FOR IN-SITU ASSEMBLIES

Two cases of pin diversion where twenty two pins have been replaced by stainless steel rods will be discussed in this section. One of the cases is identical to the single assembly case discussed in Section 6.3. This case principally had pins clustered in the low burnup region missing. The other case had a similar pattern of missing pins that were now mainly clustered in the high burnup region. Figure 24 shows the two cases with the missing pins identified. These assemblies were surrounded by 8 randomly rotated bundles (not shown in Figure 24) that had no pins missing, similar to that shown in Figure 20. The fraction of missing active fuel pins in each of these cases is about 12% of the total. Figure 25 shows the deviation of the signature from the normal condition of a full assembly. The thick line shows the average signal that was developed as described in the previous section. The two other signatures each representing one of the missing pin scenarios, clearly show deviations from the base signature.

The gamma signal drops in the vicinity of the missing pins mainly due to the loss of the local source of gammas. The drop in the gamma signal contributes to the drop in the relative ratio to a large extent. There is an increase in the thermal neutron population at the locations in the low burnup region in the vicinity of missing pins because of the migration of neutrons from the high burnup regions that are intact as well as the lack of fuel that absorbs the thermal neutrons. For

the case of missing pins in the high burnup region, there is a slight increase in the locations surrounded by a few missing pins (e.g., location 'a' with six pins missing) for reasons just discussed. The impact on the neutron population is smaller in the high burnup regions with missing pins unless a very large number of the high burnup pins is missing. The deviation of the perturbed signature from the base signature is attributable in part to the drop in the gamma signal and an increase in the neutron signal in the vicinity of the missing pins. The surrounding assemblies have a larger influence on the change in the magnitude of the neutron signal than they do on the more localized gamma signal.

A combination of the drop in the gamma signal combined with increases in the thermal neutron signal makes the relative ratio in the signature drop, leading to an overall change of shape in the signature that can be visually detected.

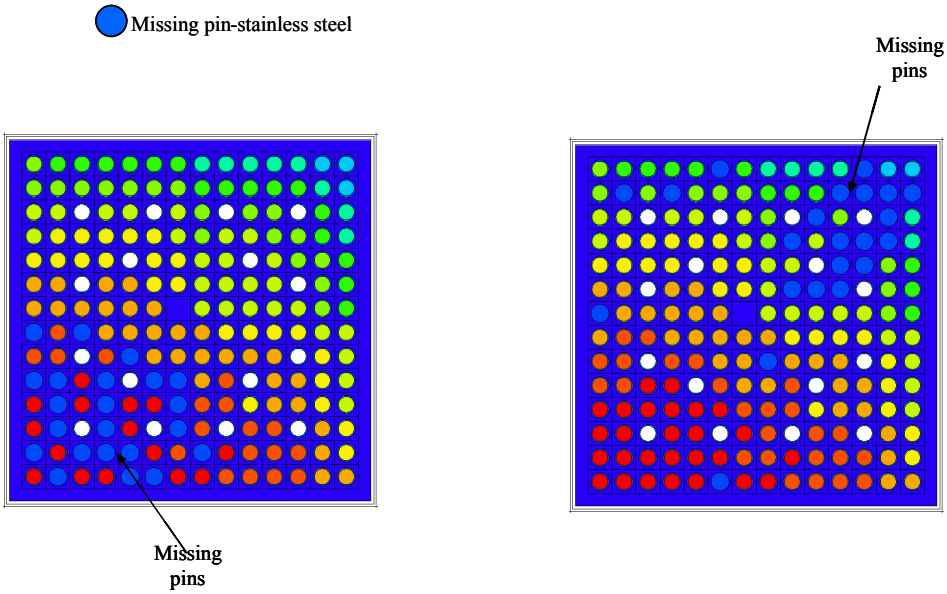


**Figure 24. Assemblies with Missing Pins**

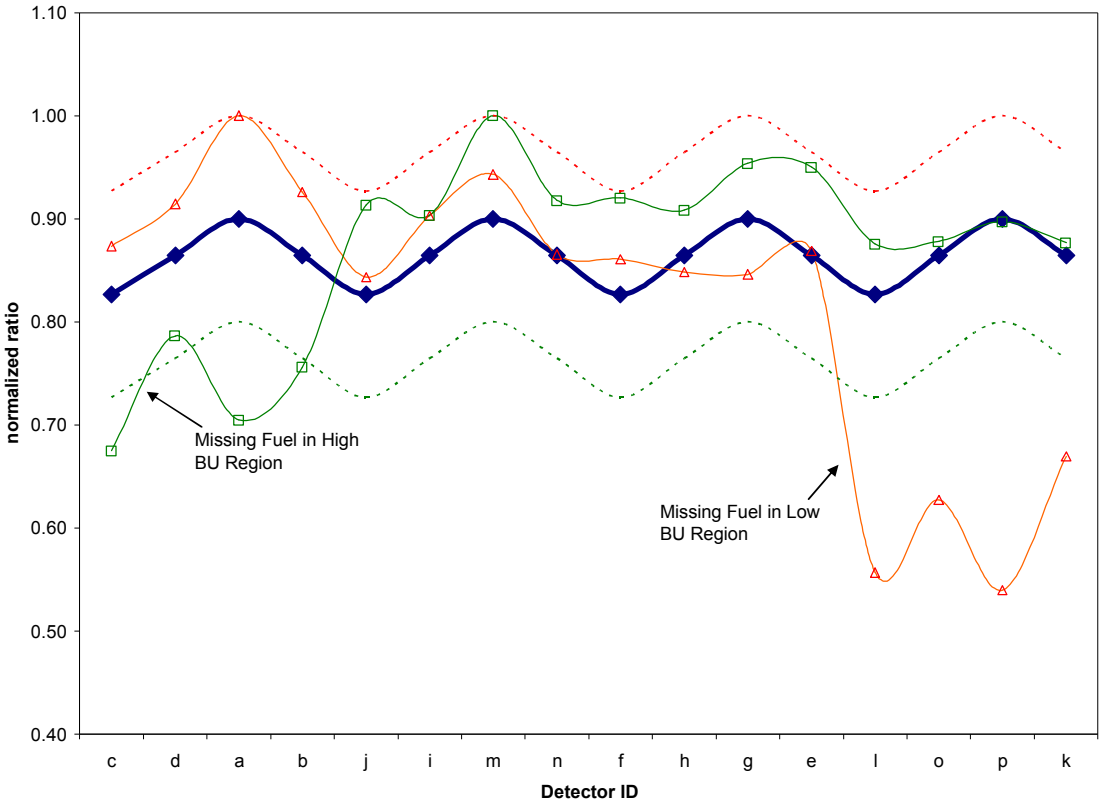


**Figure 25. Signatures with Missing Pins in Test Assembly**

Another case studied was one where the test bundle had 20 pins missing in a symmetric manner in four clusters of 5 each. The test assembly was surrounded by high and low burnup assemblies in a checkerboard manner as shown in Figure 26. The surrounding 8 fuel assemblies are alternately arranged around the test bundle with burnups of 26 and 36 MWd/kg. Figure 26 shows the test assembly with the four sets of missing fuel symmetrically arranged among the four clusters of detector sites.

Figure 27 shows the signature for this case. Seen in the Figure are the base signature for this particular case, i.e. without the 20 pins missing, as well as the standard expected the maximum and minimum curves. The base signature lies well within the maximum and minimum bounds and shows the expected shape. The signature from the diverted case shows a distinct variation from the expected curve (the error bars are the statistical uncertainty in the signal). Thus even with good symmetry, the deviation is clearly seen.

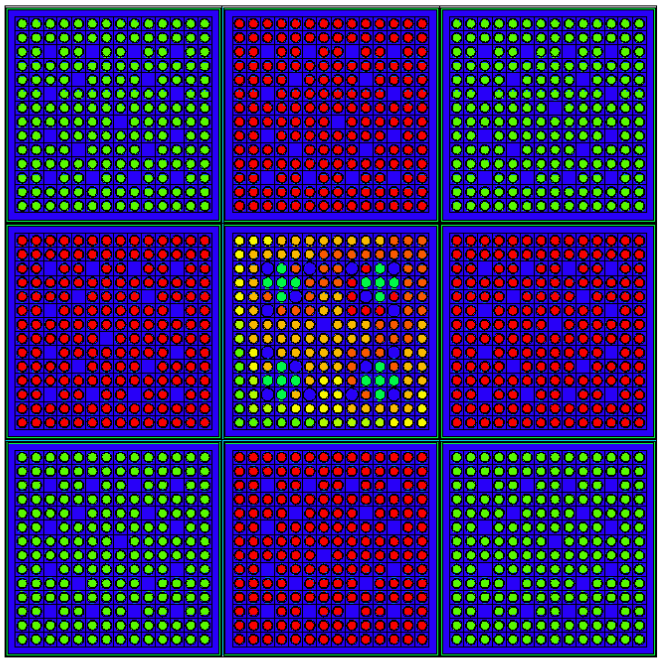

**Figure 26. Symmetrically Diverted Fuel with Checkerboard Arrangement of Surrounding Fuel**

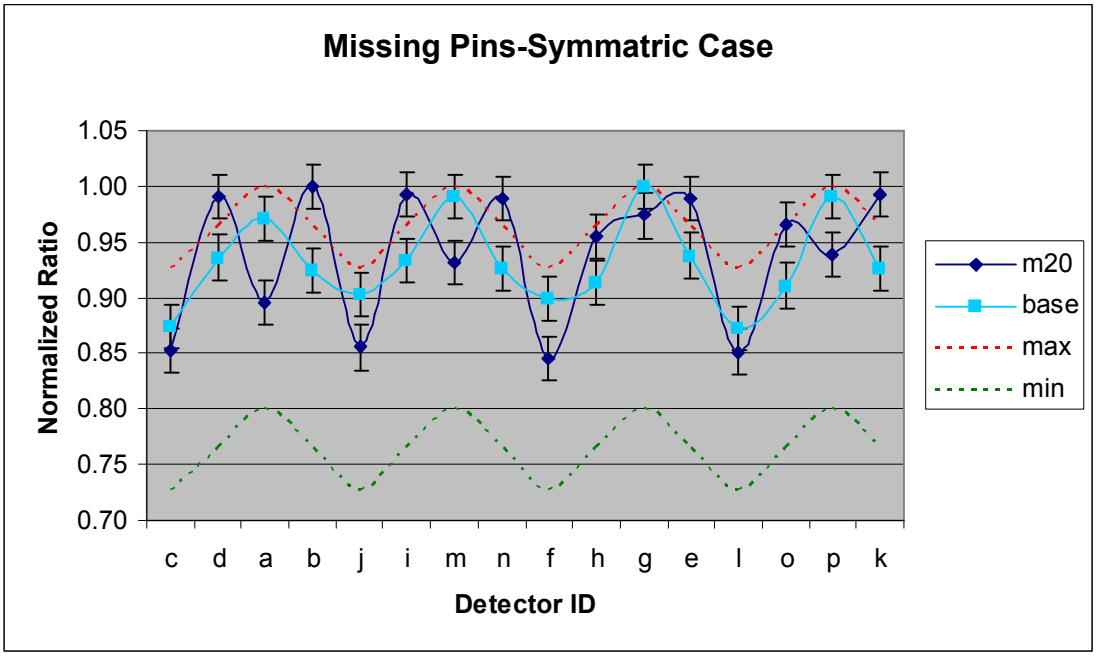


**Figure 27. Twenty Symmetrically Removed Pins**

## 10.0 CONCLUSIONS FROM SIMULATION STUDIES

Based on the simulation studies undertaken during the course of this project, the methodology developed promises to be a powerful and practical way to detect partial defects that constitute 10% or more of the total active fuel pins. This far exceeds the detection threshold of ~50% missing pins, of the currently used FDET system. The methodology does not rely on any operator provided data like burnup or cooling time and does not require movement of the fuel assembly from the storage rack in the spent fuel pool. Since the primary shape of the base signature is dependent principally on the geometric layout of the guide tubes that are quadrant symmetric, unique signatures can be developed for the various PWR fuel product lines.

Further studies are ongoing to examine the impact of symmetric removal of fuel from the assembly. Preliminary results show that since the gamma signal is fairly localized, a combination of the relative neutron, relative gamma, and relative ratio plots will still indicate diversion of 10% or more fuel pins. Further cases, particularly of symmetric removal, are being studied that point to using all three curves to determine diversion.

The next section will discuss examples of these curves by comparing the ratio as well as the normalized thermal neutron and gamma signals from simulations to measured data.

## 11.0 BENCHMARKING EXPERIMENTS

### 11.1 Description of the three PWR spent fuel assemblies used for measurements

The three spent fuel assemblies used for benchmarking measurements, discharged from an actual commercial PWR nuclear power plant, Kori-1, in Korea are currently being stored at Korea Atomic Energy Research Institute with the top nozzle removed. Basic information on the three Westinghouse 14 x 14 fuel assemblies is presented in Table17.

Figures 28-30 show the location of fuel rod, control rod guide tube and instrumentation tube for the assemblies C15, G23 and J14. Although all fuel rods were present at the time of discharge, since then many fuel rods have been removed for destructive testing. Twenty two fuel rods each were removed from assemblies C15 and G23, corresponding to 12% of the total number of fuel rods (179) in an assembly. The positions where the fuel rods were removed are shown in red and are filled with water (see Figures….). In addition, three rods were replaced by stainless steel rods in G23 (indicated by the “stars” in Figure 2). Thus, the assembly G23 has approximately 14% of the fuel rods missing. The assembly J14 has only one fuel rod missing and essentially represented a full assembly. It must be noted that the Westinghouse type 14x14 is not totally symmetric due to the presence of the instrumentation tube, which is filled with water, at the position G7. Figures 31-33 show pin- by -pin fuel rod burn-up distributions for C15, G23 and J14 assemblies.

The assemblies C15 and G23 have steep gradients of fuel burn-up, i.e., the difference in burn-up between the lowest and the highest for C15 and G23 were 35 % and 80%, respectively. The extent of the variation in G23 is unusual and represents an extreme case to test the validity of the PDET methodology.

**Table 17: Description of the three PWR spent fuel assemblies used for experiments.**

| Fuel ID | Fuel Type | Burnup (GWd/tU) | Discharge Date | Initial Enr. (%) | Number of missing rods |
|---|---|---|---|---|---|
| **C15** | WH 14x14 | 32.0 | 4/17/82 | 3.2 | 22 (12%) |
| **G23** | WH 14x14 | 35.5 | 10/24/86 | 3.2 | 25 (14%) |
| **J14** | WH 14x14 | 37.5 | 1/20/89 | 3.2 | 1 (0.6 %) |

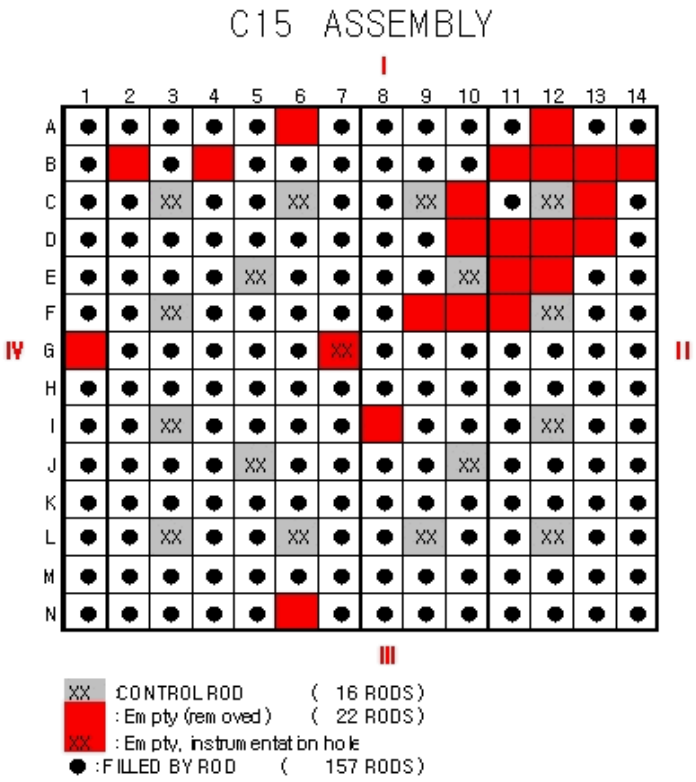


**Figure 28: Map showing the location of the fuel rods, control rod holes and instrumentation hole for the spent fuel assembly C15. The blocks colored red indicates position covered with water.**

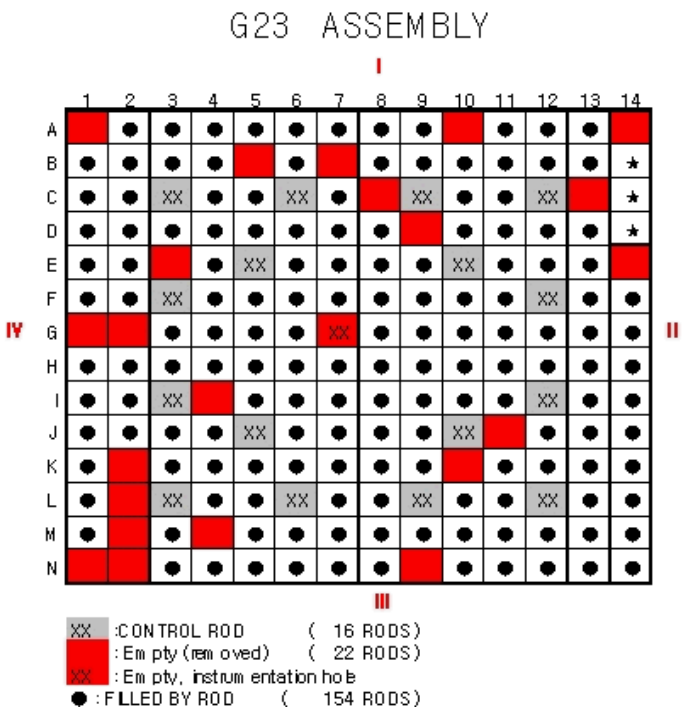


**Figure 29: Map showing the location of the fuel rods, control rod holes and instrumentation hole for the spent fuel assembly G23. The blocks colored red indicates position covered with water.**

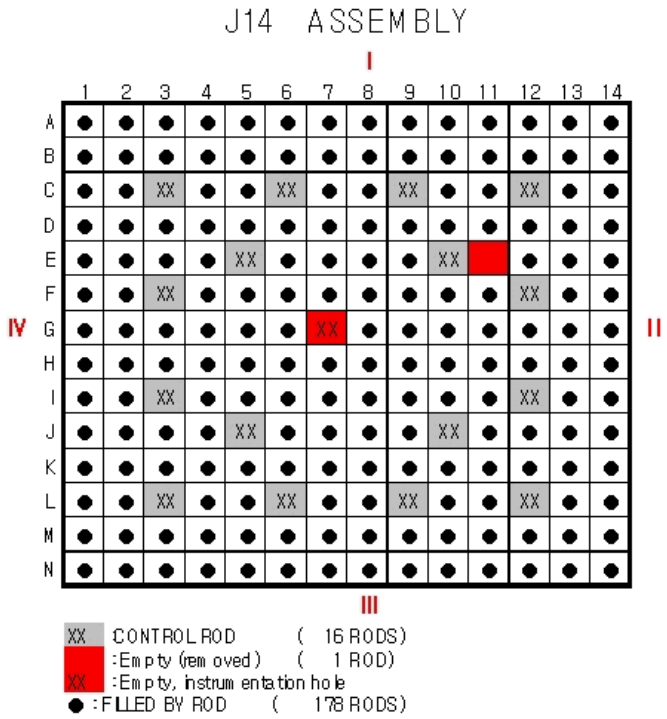


**Figure 30: Map showing the location of the fuel rods, control rod holes and instrumentation hole for the spent fuel assembly J14. The blocks colored red indicates position covered with water.**

| | 1 | 2 | 3 | 4 | 5 | 6 | 7 | 8 | 9 | 10 | 11 | 12 | 13 | 14 |
|---|---|---|---|---|---|---|---|---|---|---|---|---|---|---|
| A | 29.9 | 29.9 | 29.9 | 32.0 | 32.0 | 32.0 | 32.8 | 32.8 | 33.6 | 33.6 | 33.6 | 34.2 | 34.2 | 34.2 |
| B | 29.9 | 31.7 | 31.7 | 31.7 | 33.2 | 33.2 | 34.0 | 34.0 | 34.9 | 34.9 | 35.1 | 35.1 | 35.1 | 34.2 |
| C | 29.9 | 31.7 | xx | 33.6 | 33.6 | xx | 34.0 | 34.0 | xx | 35.8 | 35.8 | xx | 35.1 | 34.2 |
| D | 29.9 | 31.7 | 33.6 | 33.6 | 33.6 | 33.6 | 34.0 | 34.0 | 35.8 | 35.8 | 35.8 | 35.8 | 35.1 | 33.9 |
| E | 29.9 | 31.8 | 33.6 | 33.6 | xx | 33.6 | 33.1 | 33.1 | 35.8 | xx | 35.8 | 35.8 | 35.1 | 33.9 |
| F | 29.9 | 31.8 | xx | 33.6 | 33.6 | 33.6 | 33.1 | 33.1 | 35.8 | 35.8 | 35.8 | xx | 35.1 | 33.9 |
| G | 28.3 | 31.2 | 31.2 | 31.2 | 31.8 | 31.8 | xx | 33.3 | 33.2 | 33.2 | 34.2 | 34.2 | 34.2 | 33.1 |
| H | 28.3 | 31.2 | 31.2 | 31.2 | 31.8 | 31.8 | 33.3 | 33.3 | 33.2 | 33.2 | 34.2 | 34.2 | 34.2 | 33.1 |
| I | 27.5 | 30.2 | xx | 31.5 | 31.5 | 31.5 | 31.8 | 31.8 | 33.7 | 33.7 | 33.7 | xx | 33.5 | 32.4 |
| J | 27.5 | 30.2 | 31.5 | 31.5 | xx | 31.5 | 31.8 | 31.8 | 33.7 | xx | 33.7 | 33.7 | 33.5 | 32.4 |
| K | 27.5 | 28.3 | 31.5 | 31.5 | 31.5 | 31.5 | 31.1 | 31.1 | 33.7 | 33.7 | 33.7 | 33.7 | 31.8 | 32.4 |
| L | 26.0 | 28.3 | xx | 31.5 | 31.5 | xx | 31.1 | 31.1 | xx | 33.7 | 33.7 | xx | 31.8 | 30.0 |
| M | 26.0 | 38.3 | 28.3 | 28.3 | 30.0 | 30.0 | 31.1 | 31.1 | 31.7 | 31.7 | 31.8 | 31.8 | 31.8 | 30.0 |
| N | 26.0 | 26.0 | 26.0 | 27.2 | 27.2 | 27.2 | 27.9 | 27.9 | 28.6 | 28.6 | 28.6 | 30.0 | 30.0 | 30.0 |

**Figure 31: Pin by pin fuel rod burn up distribution of the assembly C15**

| | 1 | 2 | 3 | 4 | 5 | 6 | 7 | 8 | 9 | 10 | 11 | 12 | 13 | 14 |
|---|---|---|---|---|---|---|---|---|---|---|---|---|---|---|
| A | 28.2 | 27.8 | 27.5 | 27.3 | 27.1 | 27.0 | 26.9 | 25.4 | 25.3 | 25.0 | 25.0 | 24.0 | 23.2 | 22.3 |
| B | 29.6 | 29.5 | 29.7 | 29.1 | 28.9 | 29.2 | 28.7 | 27.1 | 27.4 | 26.8 | 26.3 | 26.0 | 24.8 | 23.6 |
| C | 31.0 | 31.4 | xx | 31.3 | 31.1 | xx | 30.7 | 29.0 | xx | 28.8 | 28.3 | xx | 26.5 | 24.8 |
| D | 32.1 | 32.2 | 32.8 | 32.5 | 32.8 | 32.5 | 31.5 | 29.6 | 30.3 | 30.2 | 29.3 | 28.7 | 27.2 | 25.8 |
| E | 33.2 | 33.4 | 34.0 | 34.2 | xx | 33.4 | 32.4 | 30.1 | 30.9 | xx | 30.7 | 29.7 | 28.1 | 26.7 |
| F | 34.3 | 34.9 | xx | 35.0 | 34.5 | 34.0 | 34.0 | 30.9 | 30.9 | 31.3 | 31.2 | xx | 29.2 | 27.4 |
| G | 35.1 | 35.2 | 35.7 | 34.9 | 34.4 | 34.9 | xx | 31.8 | 31.0 | 30.9 | 30.9 | 30.7 | 29.3 | 27.9 |
| H | 36.2 | 36.3 | 36.8 | 35.9 | 35.2 | 34.9 | 35.0 | 34.4 | 33.8 | 33.6 | 33.5 | 33.3 | 31.7 | 30.3 |
| I | 37.0 | 37.7 | xx | 37.8 | 37.0 | 35.8 | 34.9 | 34.7 | 34.8 | 35.2 | 35.1 | xx | 32.8 | 30.9 |
| J | 37.7 | 38.0 | 38.7 | 38.8 | xx | 37.4 | 35.9 | 35.5 | 36.3 | xx | 36.0 | 34.8 | 32.9 | 31.4 |
| K | 38.5 | 38.7 | 39.4 | 39.0 | 39.2 | 38.6 | 37.2 | 36.8 | 37.6 | 37.3 | 36.2 | 35.4 | 33.6 | 32.1 |
| L | 39.2 | 39.9 | xx | 39.8 | 39.5 | xx | 38.6 | 38.2 | xx | 37.7 | 37.0 | xx | 34.8 | 32.9 |
| M | 39.7 | 39.8 | 40.2 | 39.4 | 39.1 | 39.3 | 38.4 | 38.2 | 38.5 | 37.5 | 36.9 | 36.6 | 35.0 | 33.6 |
| N | 40.3 | 40.0 | 39.7 | 39.4 | 39.1 | 38.8 | 38.5 | 38.6 | 38.3 | 37.8 | 37.2 | 36.5 | 35.5 | 34.6 |

**Figure 32: Pin by pin fuel rod burn up distribution of the assembly G23**

| | 1 | 2 | 3 | 4 | 5 | 6 | 7 | 8 | 9 | 10 | 11 | 12 | 13 | 14 |
|---|---|---|---|---|---|---|---|---|---|---|---|---|---|---|
| A | 35.7 | 35.7 | 35.8 | 35.8 | 35.9 | 36.0 | 35.9 | 35.8 | 35.8 | 35.9 | 36.0 | 36.3 | 36.6 | 37.1 |
| B | 36.0 | 36.4 | 37.1 | 36.7 | 36.7 | 37.3 | 36.8 | 36.6 | 37.2 | 36.8 | 36.9 | 37.6 | 37.3 | 37.4 |
| C | 36.3 | 37.3 | xx | 37.9 | 38.0 | xx | 37.9 | 37.7 | xx | 38.1 | 38.2 | xx | 38.3 | 37.7 |
| D | 36.5 | 37.0 | 38.1 | 38.1 | 38.7 | 38.6 | 37.5 | 37.4 | 38.4 | 38.7 | 38.3 | 38.6 | 38.0 | 37.9 |
| E | 36.6 | 37.2 | 38.3 | 38.8 | xx | 38.3 | 37.3 | 37.0 | 38.1 | xx | 39.0 | 38.8 | 38.1 | 38.0 |
| F | 36.7 | 37.7 | xx | 38.6 | 38.3 | 37.9 | 38.0 | 37.2 | 37.2 | 38.1 | 38.8 | xx | 38.7 | 38.1 |
| G | 36.6 | 37.1 | 38.0 | 37.5 | 37.2 | 37.9 | xx | 37.6 | 36.6 | 36.9 | 37.7 | 38.6 | 38.1 | 38.0 |
| H | 36.5 | 37.0 | 37.9 | 37.4 | 37.0 | 37.1 | 37.6 | 36.8 | 36.5 | 36.8 | 37.6 | 38.5 | 38.0 | 37.9 |
| I | 36.5 | 37.6 | xx | 38.4 | 38.0 | 37.1 | 36.6 | 36.4 | 36.9 | 38.0 | 38.7 | xx | 38.5 | 37.9 |
| J | 36.4 | 37.0 | 38.1 | 38.5 | xx | 37.9 | 36.8 | 36.7 | 37.8 | xx | 38.8 | 38.7 | 38.0 | 37.8 |
| K | 36.3 | 36.9 | 37.9 | 37.9 | 38.5 | 38.3 | 37.3 | 37.2 | 38.3 | 38.6 | 38.2 | 38.5 | 37.9 | 37.7 |
| L | 36.3 | 37.3 | xx | 37.9 | 38.0 | xx | 37.8 | 37.7 | xx | 38.1 | 38.2 | xx | 38.9 | 37.7 |
| M | 36.1 | 36.5 | 37.2 | 36.8 | 36.9 | 37.4 | 36.9 | 36.8 | 37.4 | 36.9 | 37.1 | 37.8 | 37.4 | 37.5 |
| N | 36.0 | 36.0 | 36.2 | 36.2 | 36.2 | 36.3 | 36.3 | 36.2 | 36.2 | 36.3 | 36.4 | 36.7 | 36.9 | 37.4 |

**Figure 33: Pin by pin fuel rod burn up distribution of the assembly J14**

## 11.2 Selection of Neutron Detector

As a component of this project, a small neutron detector must be developed or purchased if commercially available, that can fit inside the control rod guide tube of a spent fuel assembly as it stands on the bottom of a cooling pond. The detector must have a diameter much less than 1cm in order to fit inside the guide tube. In addition, the detector must possess some other important qualities such as excellent neutron/gamma discrimination, ruggedness, and resistance to radiation damage. Inside a spent fuel assembly, the gamma activity is approximately 7 orders of magnitude higher than the neutron activity. As such, an accurate measurement of the neutron flux will require a precise degree of neutron/gamma discrimination.

Scintillators:

The use of scintillators is not recommended. Even if a scintillating material could be found which achieved the required neutron/gamma discrimination (e.g. ZnS coupled with LiF), the associated PMT would still be a problem. All PMT's are inherently sensitive to gammas due to the hi-z photocathode material. Furthermore, the tight constraint on the instrument diameter would make the use of PMT's problematic in the first place. One possible fix would be to optically couple the scintillator to a remote and well shielded PMT, but this could greatly lower the sensitivity of the instrument.

Self-powered detectors:

Self- powered detectors for neutron measurements are based on the beta decay that captured neutrons generate beta currents which can be measured directly without external bias voltage. The current is proportional to the rate at which neutrons are captured in the detector. The use of self-powered detectors may be difficult due to relatively low neutron flux in the old spent fuel environment.

Solid state detectors:

The use of solid state detectors (e.g. B4C) is not recommended due to radiation damage issues in the high gamma ray flux.

Fission chamber:

This is likely the best option. A fission chamber takes advantage of the enormous Q-value in neutron induced fission (~ 200 MeV), and a high thermal neutron cross section, to provide unparalleled neutron/gamma discrimination. Photon induced fission is not a problem due to the high energy thresholds and low cross sections that are involved. A fission chamber can easily meet the constraints regarding size and radiation hardness. It may also be possible to count both thermal and fast neutrons by using two separate chambers and coating one with U-235 (thermal fissioner) and the other with U-238 (fast fissioner, 1 MeV threshold). However, since the fast fission cross section of U-238 is 1000 times lower than the thermal fission cross section of U-235, hyper-pure U-238 must be used (<0.1% U-235). The lower cross section will also affect the neutron/gamma discrimination for fast neutrons.

BF3 tubes:

The $^{10}B$(n,alpha) reaction has a reasonably high Q-value (~2 MeV), and large thermal neutron cross section, both of which enable neutron/gamma discrimination. However, the Q value is still lower than that of fission, and thus the neutron/gamma discrimination will not be as good as a fission chamber. Furthermore, it is not clear how well thermal neutrons can be differentiated from fast neutrons. The approach would be to set the discriminator higher in the case of fast neutrons, but the fast cross section is 4 orders of magnitude lower.

Compensated ion chambers (CIC's):

Compensated ion chambers use two ion chambers from which two independent ion currents can be generated. One chamber is boron lined in its inner surface for neutron measurements and the other chamber, which is almost identical to the first chamber in terms of its geometry and material, is without the boron lining for gamma measurements. The gamma flux information is obtained with the second ion chamber, but the neutron flux information can be obtained by taking a difference in current between the first ion chamber and second chamber. In general, the two chambers may not have identical response to gamma ray flux. This variation may require adjustments in the balance between the tow chambers to restore exact compensation for different gamma-ray flux levels. Additional difficulty for safeguards application is due to relatively lower neutron and gamma flux in the spent fuel measurement environment compared to the reactor power measurement environment. Advantage of using CTC would be the simultaneous information gathering of both neutron and gamma information from a spent fuel assembly.

Considering various options for neutron measurement for PWR spent fuel assemblies, initial choice would be a fission chamber due to its ruggedness, high neutron/gamma discrimination, high resistance to radiation damage and commercial availability.

### 11.3 Data Acquisition

Neutron measurement experiments were conducted using a miniature neutron detector which was placed into a thin stainless steel tube. The technical information of the fission chamber is shown in the Table 18. This tube was inserted, in turn, into each of the guide tubes for neutron measurements, generating 16 pulse height spectra for each assembly. The measurement data were obtained in a pulse height spectrum format with 1024 channels. All measurements were obtained at 150 cm below from the top of the fuel assembly with the measurement time of 100 seconds. In addition, a total of 11 spectra were obtained at multiple depths at the guide tube position L-12 of the assembly J14 to measure neutron and gamma radiation levels. The measurements were taken with MMCA (Mini Multi-Channel Analyzer), the standard IAEA MCA, and WinSPEC, one of the standard pieces of software at the Department of Safeguards at IAEA. The main advantage of using this hardware and software is that there would be no training required for IAEA inspectors as the electronics and the software are already being widely used at IAEA.

**Table 18: Technical specification of the Centronics FC4A a miniature neutron detector used for measurements.**

| | |
|---|---|
| Maximum Diameter (mm) | 6.2 |
| Maximum Length (mm) | 45.25 |
| Effective Length (mm) | 25 |
| Fill Gas | Argon + 2% Nitrogen |
| Fill Pressure (psi/atm) | 75/ 5.1 |
| Operating voltage | 500 V |
| Connector | SHV |
| Fissile coating material | U3O8 (93% enriched) |
| Fissile coating density | 1 mg/cm^2 |
| Neutron sensitivity | 3x10^3 cps/nv |

## 12.0 RESULTS AND DISCUSSION

### 12.1 Neutron Signatures

To obtain neutron counts, the threshold was applied to all measured spectra at channel 200 which is high enough to ensure that no gamma pile up effect is influencing the neutron counts. Example spectra are shown in Figure 34 for the measurements taken at the depth of 150 cm, 100 cm, 50 cm and 0 cm from the top of the spent fuel assembly J14 at the position L12. The axial neutron and gamma profiles are also shown in Figure 35. As the measurement position moves deeper, the neutron as well as gamma radiation level increases. The reduction of the neutron level at 150 cm is due to the presence of the grid near this depth.

Table 19 shows both experimental neutron data and MCNP simulated data which are normalized to the maximum value of the each assembly, as well as the raw data for measurements. Figures 36-38 show the comparison between the experimental data and simulated data for all three assemblies. For the most part the MCNP and experimental data were within 0.05 of each other with a small number agreeing within 0.1. Overall, it is concluded that the MCNP simulated data agreed extremely well with the measured data, thus providing good validation of the simulation methodology.

Note on the plot and error bars: The statistical uncertainty at the 1-σ level for the ratio is between 1 and 2 percent for the MCNP simulation. All measurement errors are less than 5%. For the sake of clarity, the statistical uncertainties and the measurement errors are not shown in these subsequent plots. The Figure 36 is shown with error bars for an example.

On the safeguards verification note, an inspector can easily conclude that the PWR spent fuel assembly C15 is disturbed without even having the detailed knowledge of the C15 assembly as the measured neutron signature severely deviated from the expected neutron signature (base signature in green color) which is cyclic and symmetric. The inspector can also suspect that the spent fuel rods in the 4th quadrant are quite different from the rest of the fuel rods arrangement as there were increases in the neutron flux in the 4th quadrant. Note that the amount of diversion in this case was 12% whereas the current IAEA criterion for partial defect testing is 50%. For the verification of G23, the neutron profile also deviated from the neutron base profile and it lacked the smooth symmetric pattern, an indication of disruption of the fuel integrity. For J14, the deviation of the neutron is only slight for the data point E5, but it kept the smooth repetitive symmetric pattern in essence.

On an interesting note, close observation of Figure 38 discloses that the only difference between the measured plot and simulated plot is in the location of the highest peak. Investigation revealed that the facility staff erroneously reported the missing pin location at E11 rather than its true location at D5. As the MCNP simulation was performed with the data provided by the facility, the location of the peak obtained by measurements did not match the simulation profile. Although this small error was relatively less important in terms of material accounting, this finding demonstrates the effectiveness of the methodology, and the instrument, if available, could be potentially a very powerful tool for IAEA inspectors for verification of a spent fuel assembly to the partial defect level. Note that the neutron measurement was sensitive enough to identify the scenario of the single pin missing, at least in this case, whereas the existing tool cannot even tell if 50% of the spent fuel is missing or replaced with dummy fuel pins.

A MCNP case was run on the J14 with the corrected information that the missing location was at D5. The neutron profile obtained with this new MCNP matched very well with the measured neutron profile as shown in Figure 39.

**Table 19: Neutron measurement and MCNP simulated data for the assembly C-15, G23 and J14. The experimental data were obtained with the measurement time of 100 seconds.**

| | Neutron Measurem't: C15 | | Sim'n Data | Neutron Measurem't:G23 | | Sim'n Data | Neutron Measurem't: J14 | | Sim'n Data |
|---|---|---|---|---|---|---|---|---|---|
| Det Pos | Raw 100 s | Rel. Value | Rel. Value | Raw 100 s | Rel. Value | Rel. Value | Raw 100 s | Rel. Value | Rel. Value |
| J5 | 555 | 0.38 | 0.41 | 1097 | 0.89 | 0.84 | 1343 | 0.85 | 0.87 |
| I3 | 554 | 0.38 | 0.38 | 1184 | 0.96 | 0.89 | 1304 | 0.83 | 0.81 |
| L3 | 401 | 0.27 | 0.32 | 1170 | 0.94 | 1.00 | 1084 | 0.69 | 0.71 |
| L6 | 553 | 0.38 | 0.39 | 1030 | 0.83 | 0.77 | 1291 | 0.82 | 0.81 |
| J10 | 606 | 0.41 | 0.43 | 1239 | 1.00 | 0.97 | 1410 | 0.90 | 0.87 |
| L9 | 562 | 0.38 | 0.39 | 1010 | 0.82 | 0.81 | 1299 | 0.83 | 0.81 |
| L12 | 470 | 0.32 | 0.34 | 866 | 0.70 | 0.63 | 1108 | 0.71 | 0.71 |
| I12 | 626 | 0.43 | 0.40 | 912 | 0.74 | 0.68 | 1271 | 0.81 | 0.82 |
| E5 | 674 | 0.46 | 0.42 | 994 | 0.80 | 0.69 | 1571 | 1.00 | 0.88 |
| C6 | 617 | 0.42 | 0.42 | 892 | 0.72 | 0.66 | 1387 | 0.88 | 0.81 |
| C3 | 553 | 0.38 | 0.38 | 700 | 0.56 | 0.53 | 1165 | 0.74 | 0.71 |
| F3 | 592 | 0.40 | 0.39 | 1009 | 0.81 | 0.81 | 1330 | 0.85 | 0.82 |
| E10 | 1462 | 1.00 | 1.00 | 870 | 0.70 | 0.65 | 1436 | 0.91 | 1.00 |
| F12 | 1193 | 0.82 | 0.75 | 794 | 0.64 | 0.57 | 1305 | 0.83 | 0.88 |
| C12 | 1339 | 0.92 | 0.90 | 755 | 0.61 | 0.53 | 1122 | 0.71 | 0.73 |
| C9 | 866 | 0.59 | 0.58 | 951 | 0.77 | 0.76 | 1285 | 0.82 | 0.82 |

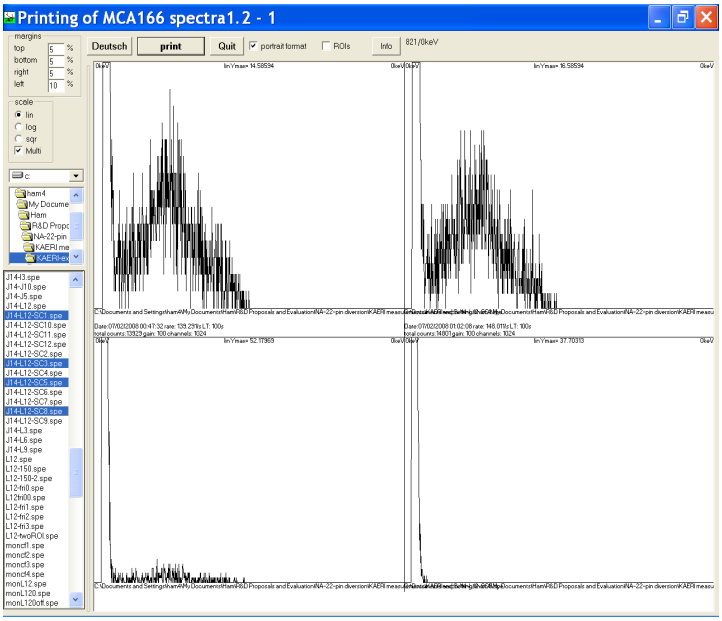


**Figure 34: Measured pulse height spectra at the depth of 150 cm, 100cm, 50 cm and 0 cm from the top of the PWR fuel assembly whose top nozzle was removed.**

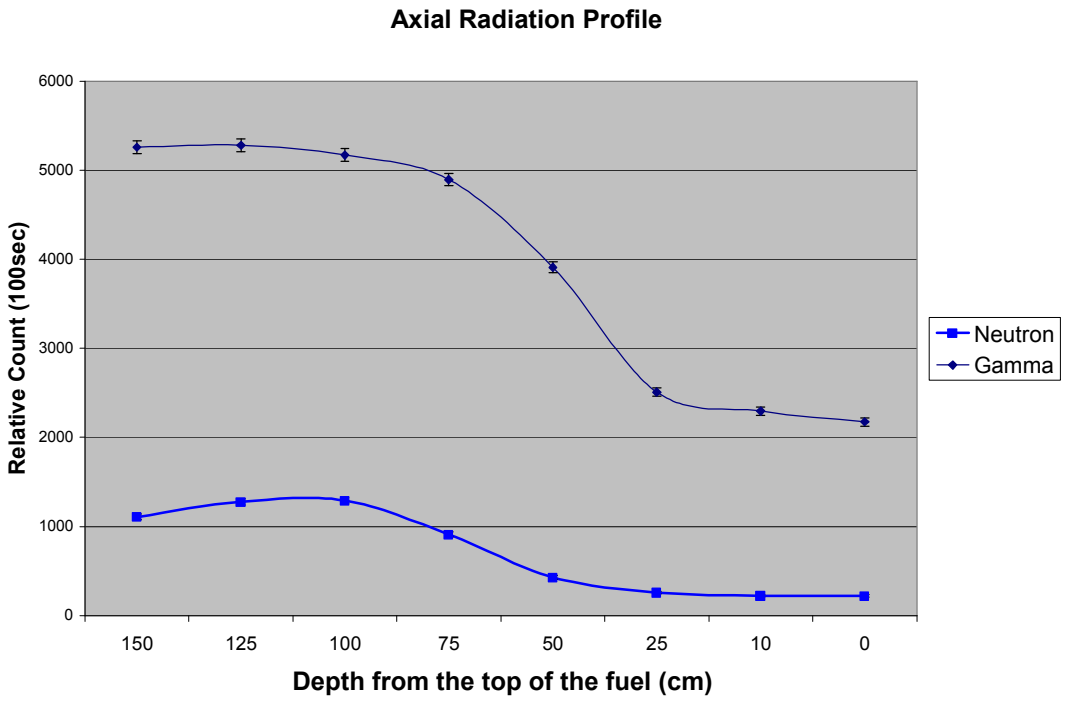


**Figure 35: Axial neutron profile of the spent fuel assembly J14 at the position L12.**

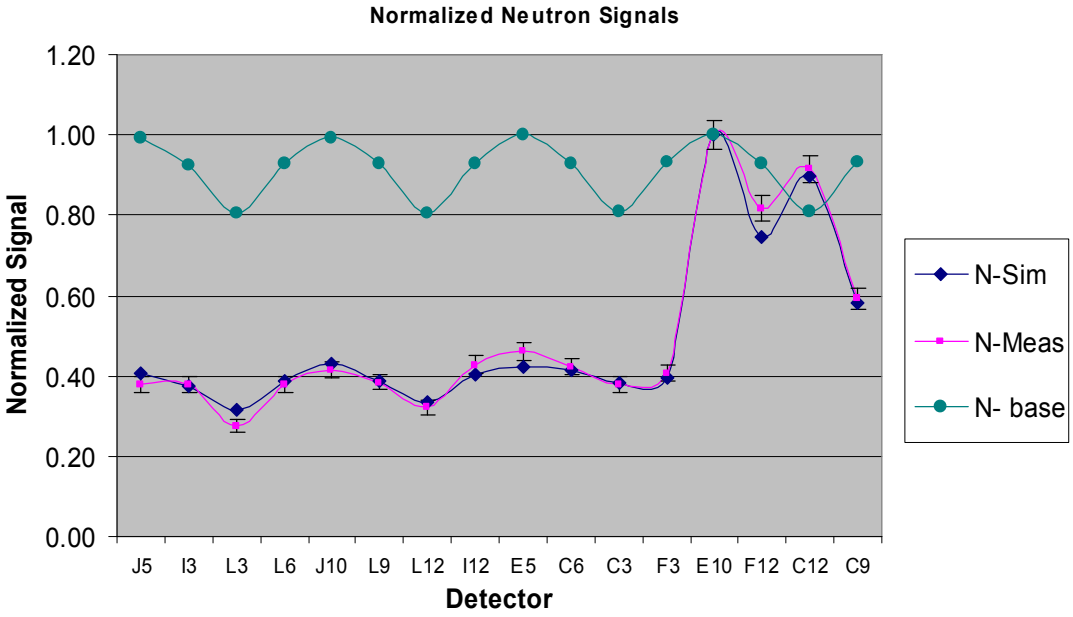


**Figure 36: Comparison of the experimental neutron data to the MCNP simulated data for the assembly C15. The N-base profile shows the case where there was no diversion. The measured signature shows the deviation from the N-base profile leading to conclusion that the assembly C15 was tampered from the original status.**

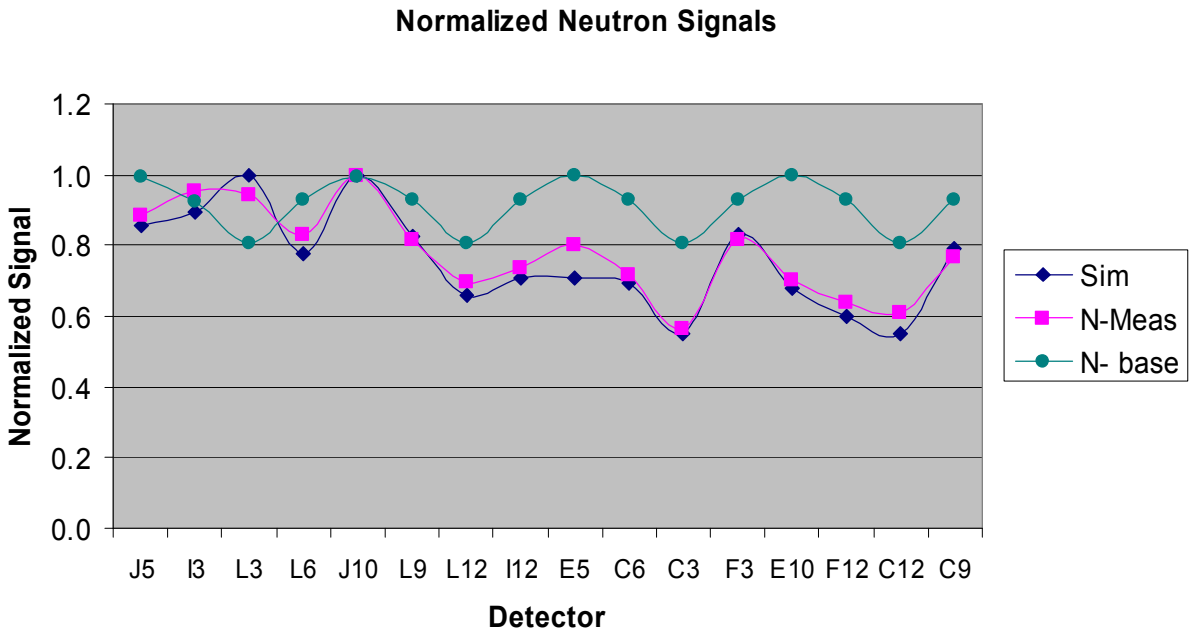


**Figure 37: Comparison of the experimental neutron data to the MCNP simulated data for the assembly G23**

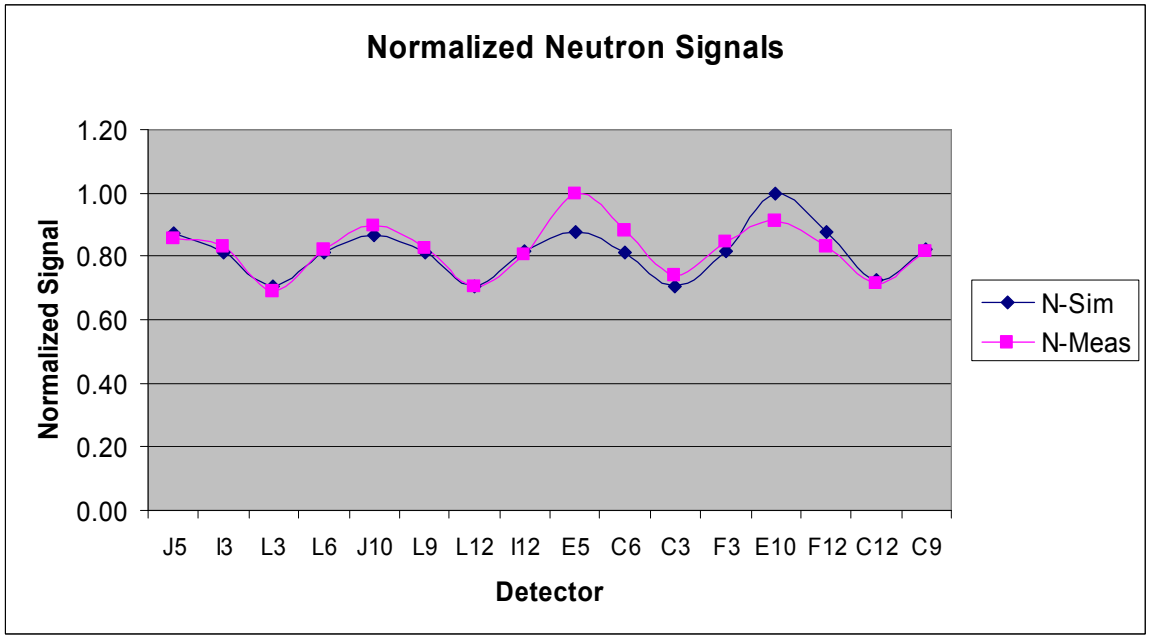


**Figure 38: Comparison of the experimental neutron data to the MCNP simulated data for the assembly J14. The discrepancy between the MCNP simulated data and measurement data were caused by the misreport of the removed fuel pin location by the facility operator. The actual position of the removed pin was right next to E5 rather than the position next to E10.**

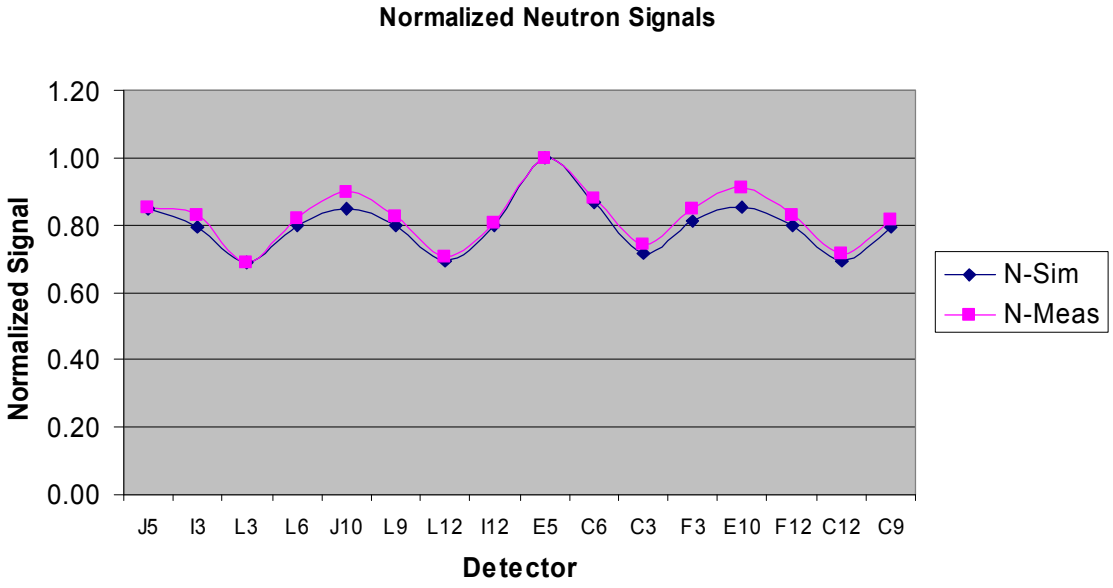


**Figure 39: Comparison of the experimental neutron data to the MCNP simulated data for the assembly J14. The new MCNP results were obtained with the corrected mission rod location. They matched fairly well.**

### 12.2 Gamma Signatures

Gamma signatures indicating gamma flux were obtained making use of the pulse height spectra acquired by the fission chamber. As the method to extract gamma flux from these spectra is in the early stage of development, it needs to be yet rigorously tested and fully demonstrated. However, initial results based on this method looked promising and reported here are the results based on the method. Whether the final instrument will use this method or another type of detector for gamma measurements such as ion chamber still needs to be determined. A few data points out of this method appear to be outliers, which were probably caused due to noise in the low energy region during measurements. The neutron data out of these pulse height spectra were fine because the threshold took care of these noises in the low energy region.

The fission chamber that was used to obtain pulse height spectra is basically an ion chamber filled with ionizing gas (Argon and 2% Nitrogen) and coated with highly enriched uranium oxide in its inner surface for thermal neutron measurements. When a neutron causes fission in the uranium oxide, fission fragments are created with high energy in the order 200 MeV, which in turn creates pulses that corresponds high energy. This energy is sufficiently high enough such that all pulses generated from alpha particles and gammas are discriminated from neutron signals when an appropriate threshold is applied. For this reason, the fission chamber was a very popular neutron detector in an extremely high radiation environment.

Although gamma signals are typically ignored in measuring neutron measurement by a fission chamber, the gamma signals are still registered in the low energy region. As alphas are always present in the relatively lower energy region (< 5~6 MeV) in the measured spectra, the gamma

signals will overlap to the alpha signals. If measurements were made in high gamma radiation environment with a system that can capture every gamma as a pulse, a pulse height spectrum due to gamma can be obtained when the alpha spectrum is stripped from the measured spectrum. What makes this process challenging is the fact that significant amount of pile-up and probable preamplifier saturation occurs in the extremely high gamma environment.

Figure 40 shows multiple pulse height spectra obtained by the fission chamber in the low energy region which represents the contribution from mostly alphas and gammas only. Note that the spectra SC1 is obtained at the depth of 150 cm from the top of the spent fuel assembly, SC2 at 125 cm, SC3 at 100 cm, SC4 at 75, SC5 at 50 cm, SC6 at 25 cm, SC7 at 10 cm and SC8 at 0 cm. As the measurement position moves deeper, the gamma radiation level increases. For example, gamma level at measurement position SC1 or SC2 is much higher than that at SC8. Because of the extremely high gamma radiation, saturation in the preamplifier as well as significant pile-up is suspected to occur in the lower energy region.

Pile-up occurs when two pulses are sufficiently close together such that they are treated as a single pulse by the analysis system. The pile-up of the two full energy pulses effectively removes both from the proper position in the pulse height spectrum and creates a new position in the higher energy region (higher channel). During the measurement by the fission chamber, these pileups do occur and the amount of pile-ups depends upon the amount of incoming radiation to the detector. The number of alpha pulses coming into the measurement remains same as the alphas come from the uranium oxide inside the fission chamber. Comparing the radiation measurement without gamma radiation and the measurement with gamma radiation, it is possible to evaluate the gamma flux. Simple difference between the two spectra would not be a good estimator to estimate the gamma flux because of pile-ups, noise and probable saturation particularly in the low energy region. This is evident in the multiple spectra shown in the Figure 40. For this reason, the choice of region of interest (ROI) needs to be beyond the peak of the spectra obtained in the highest radiation environment. For the estimation of the gamma flux, the ROI applied was between channels 34-50. All measured pulse height spectra were treated with this ROI and the relative gamma flux values are plotted against the measurement positions as shown in Figures 41-43. Table 20 presents comparisons between the measurement and MCNP simulation normalized gamma signal. It is noted that the normalization is performed using the largest signal other than the obviously spurious signal. Other than the spurious signals, the results from both sets for each assembly are within 0.10, once again suggesting that the simulation model used is a valid one.

Although it appears that there are multiple outliers in estimating gamma flux, overall the method matched reasonably well, an encouraging sign to further explore this approach. The use of this approach is significantly advantageous as the method requires neither additional detectors nor an instrument for gamma measurements.

On the safeguards verification note, unlike the verification using the neutron signatures, the gamma profiles alone is not recommended to be used for verification as the gamma flux theoretically could come from other gamma sources. However, the gamma profile will provide complementary measure or additional information to detect any symmetric diversion of spent fuel rods.

**Table 20: Gamma measurement and MCNP simulated data for the assembly C-15, G23 and J14. The gamma data were obtained extracting the information from the pulse height spectra acquired by a fission chamber.**

| | Measurement Data | | MCNP Data | Measurement Data | | MCNP Data | Measurement Data | | MCNP Data |
|---|---|---|---|---|---|---|---|---|---|
| Det Pos | G-C15 | Rel. Value | Rel. Value | G-G23 | Rel. Value | Rel. Value | G-J14 | Rel. Value | Rel. Value |
| J5 | 2464 | 0.94 | 0.95 | 3033 | 0.95 | 1.00 | 3601 | 1.04 | 1.00 |
| I3 | 2215 | 0.85 | 0.91 | 3043 | 0.96 | 0.95 | 4242 | 1.22 | 0.97 |
| L3 | 2215 | 0.85 | 0.82 | 2654 | 0.83 | 0.84 | 3075 | 0.88 | 0.92 |
| L6 | 2336 | 0.90 | 0.89 | 3182 | 1.00 | 0.99 | 3320 | 0.95 | 0.97 |
| J10 | 2832 | 1.09 | 1.00 | 3093 | 0.97 | 0.95 | 3423 | 0.98 | 1.00 |
| L9 | 2431 | 0.93 | 0.93 | 3034 | 0.95 | 0.95 | 3378 | 0.97 | 0.97 |
| L12 | 2274 | 0.87 | 0.91 | 2747 | 0.86 | 0.90 | 3048 | 0.88 | 0.92 |
| I12 | 2608 | 1.00 | 0.97 | 2736 | 0.86 | 0.88 | 3301 | 0.95 | 0.97 |
| E5 | 2533 | 0.97 | 0.99 | 4366 | 1.37 | 0.89 | 3479 | 1.00 | 1.00 |
| C6 | 2538 | 0.97 | 0.95 | 2501 | 0.79 | 0.76 | 3386 | 0.97 | 0.97 |
| C3 | 2121 | 0.81 | 0.86 | 2358 | 0.74 | 0.77 | 3037 | 0.87 | 0.92 |
| F3 | 2354 | 0.90 | 0.93 | 2650 | 0.83 | 0.87 | 3510 | 1.01 | 0.97 |
| E10 | 2190 | 0.84 | 0.90 | 2687 | 0.84 | 0.80 | 3547 | 1.02 | 0.98 |
| F12 | 3598 | 1.38 | 0.90 | 2456 | 0.77 | 0.77 | 3467 | 1.00 | 0.96 |
| C12 | 1779 | 0.68 | 0.73 | 2133 | 0.67 | 0.60 | 3129 | 0.90 | 0.92 |
| C9 | 2975 | 1.14 | 0.91 | 2300 | 0.72 | 0.74 | 3359 | 0.97 | 0.96 |

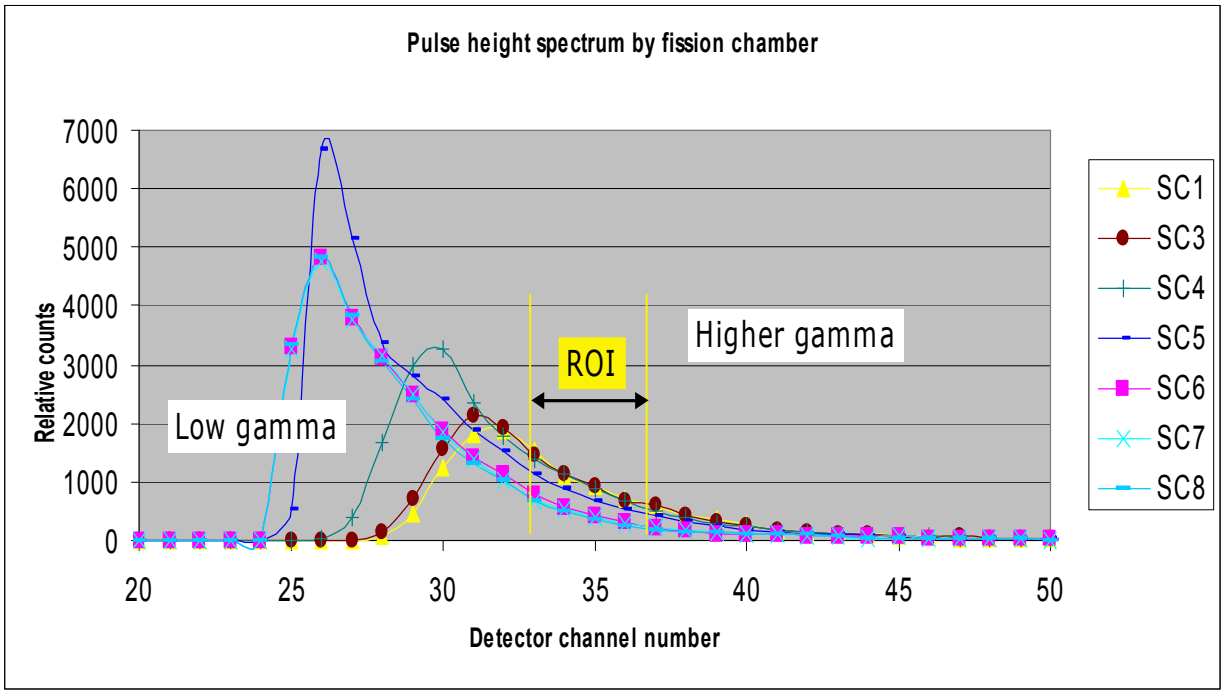


**Figure 40: Pulse height spectra al the different depths (different gamma flux). The spectra are obtained at the multiple depths inside a spent fuel assembly.**

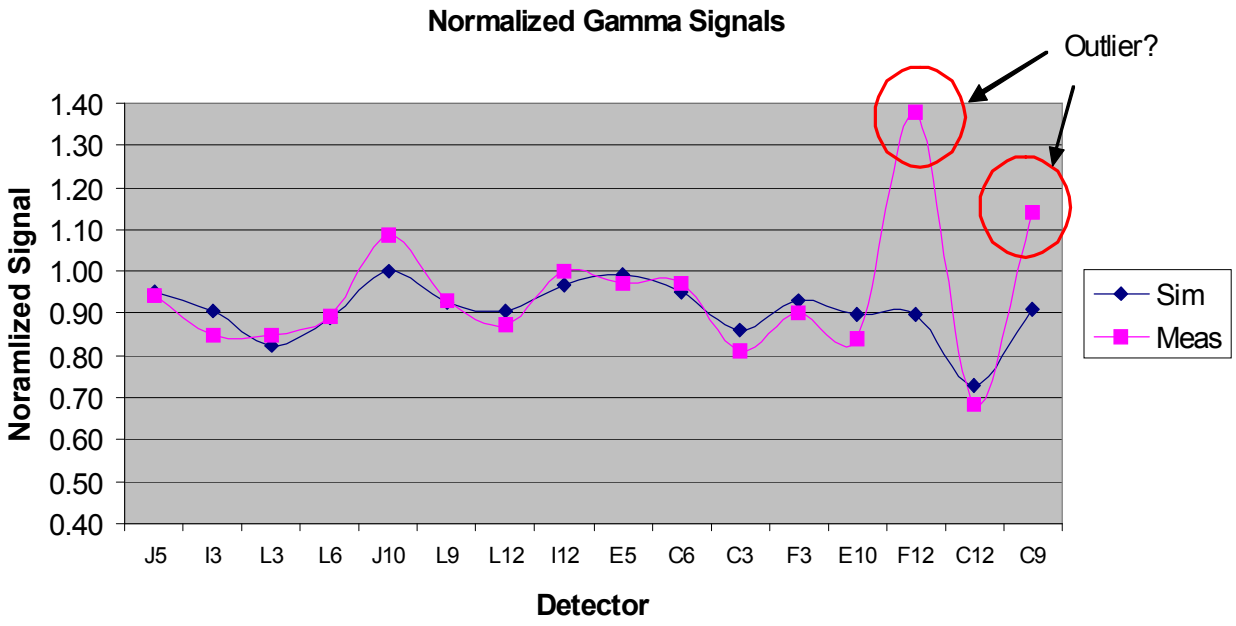


**Figure 41: Comparison of the experimental gamma data to the MCNP simulated data for the assembly C15. There are two points appeared to be outliers probably due to noise in the low energy region during measurements.**

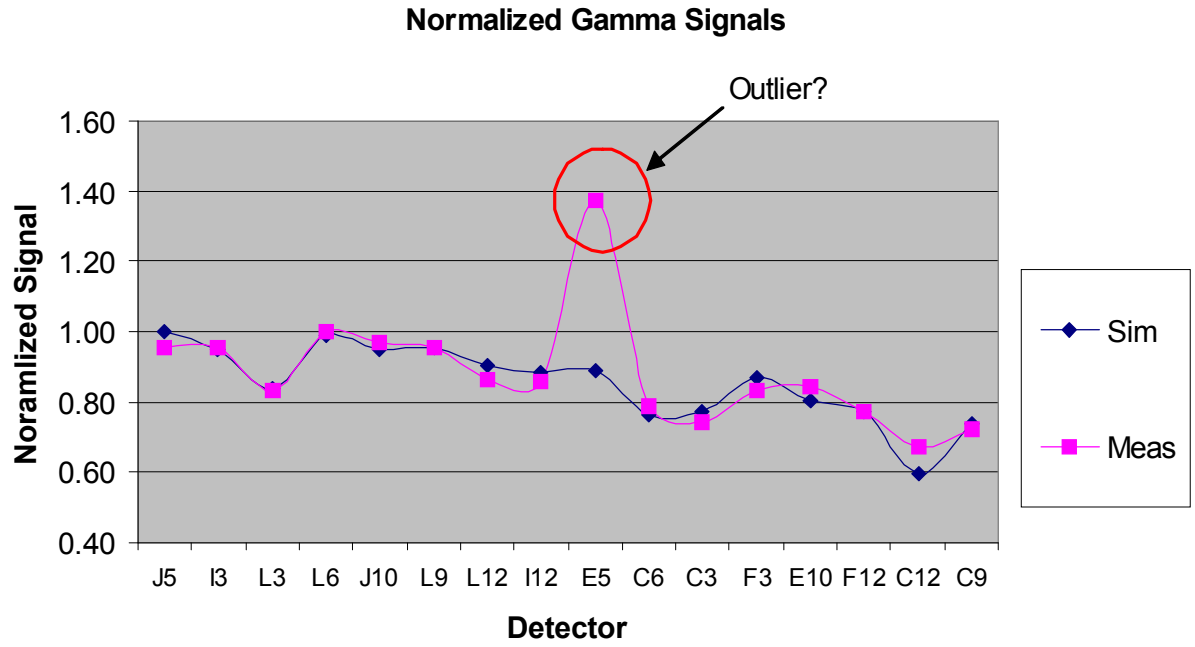


**Figure 42: Comparison of the experimental gamma data to the MCNP simulated data for the assembly G23. The outlier data point is probably caused by the noise in the low energy region during measurement.**

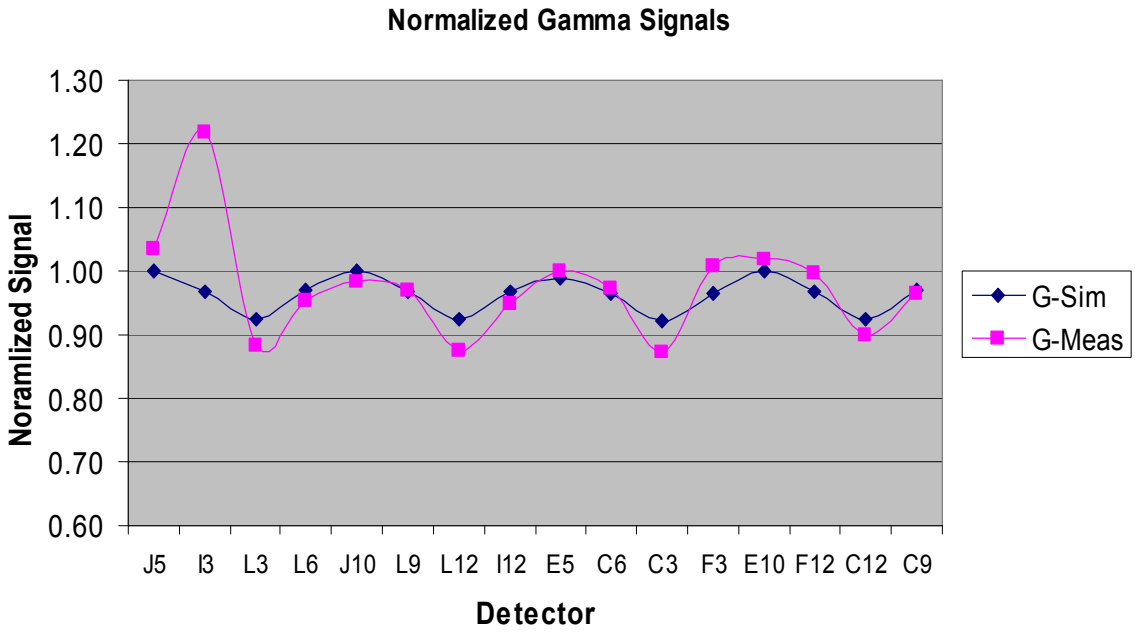


**Figure 43: Comparison of the experimental gamma data and MCNP simulated data for the assembly J14. The outlier data point is probably caused by the noise in the low energy region during measurement.**

### 12.3 Gamma/Neutron Ratio Signatures

The normalized ratios, defined as normalized gamma to thermal neutron ratios, are plotted against the measurement positions (guide tube positions) in Figures 44-46. Table 21 presents the normalized ratios for the three assemblies. Once again other than the differences caused by the spurious gamma signals, the agreement is generally within 0.1 for all assemblies. Given the good agreement between experiment and the simulation model for all three signals, the validity of the simulation technique has been proven.

On the safeguards verification note, an inspector can easily conclude, just as with the neutron signature alone, that the PWR spent fuel assembly C15 is disturbed without even having any detailed knowledge of the C15 assembly as the measured ratio signature severely deviated from the expected ratio base signature (shown in green) which is cyclic and symmetric. The inspector can also suspect that the spent fuel rods in the 4th quadrant are quite different from the rest of the fuel rods arrangement. For the verification of G23, the measured ratio signature also deviated from the ratio base signature and it lacked the smooth symmetric pattern, an indication of disruption of the fuel integrity. For J14, the measured ratio signature deviates only slightly except the second data point which was caused by the spurious gamma signal (discussed in the earlier section), but it kept the smooth repetitive symmetric pattern in essence. Although the percentage of diverted pins for both C15 and G23 was well below the current IAEA criterion for partial defect testing of 50%, the methodology was able to clearly detect the diversion.

**Table 21: Gamma/Neutron Ratio data from measurement and MCNP simulated data for the assembly C-15, G23 and J14.**

| | Measurement Data | | MCNP Data | Measurement Data | | MCNP Data | Measurement Data | | MCNP Data |
|---|---|---|---|---|---|---|---|---|---|
| Det Pos | G-C15 | Rel. Value | Rel. Value | G-G23 | Rel. Value | Rel. Value | G-J14 | Rel. Value | Rel. Value |
| J5 | 4.44 | 0.92 | 0.86 | 2.76 | 0.82 | 0.83 | 2.68 | 0.95 | 0.88 |
| I3 | 4.00 | 0.83 | 0.89 | 2.57 | 0.76 | 0.75 | 3.25 | 1.15 | 0.91 |
| L3 | 5.52 | 1.14 | 0.96 | 2.27 | 0.67 | 0.60 | 2.84 | 1.00 | 1.00 |
| L6 | 4.22 | 0.87 | 0.85 | 3.09 | 0.92 | 0.91 | 2.57 | 0.91 | 0.91 |
| J10 | 4.68 | 0.97 | 0.86 | 2.50 | 0.74 | 0.67 | 2.43 | 0.86 | 0.88 |
| L9 | 4.33 | 0.89 | 0.89 | 3.00 | 0.89 | 0.83 | 2.60 | 0.92 | 0.91 |
| L12 | 4.84 | 1.00 | 1.00 | 3.17 | 0.94 | 1.00 | 2.75 | 0.97 | 1.00 |
| I12 | 4.17 | 0.86 | 0.89 | 3.00 | 0.89 | 0.88 | 2.60 | 0.92 | 0.91 |
| E5 | 3.76 | 0.78 | 0.87 | 4.39 | 1.30 | 0.89 | 2.21 | 0.78 | 0.87 |
| C6 | 4.11 | 0.85 | 0.85 | 2.80 | 0.83 | 0.79 | 2.44 | 0.86 | 0.91 |
| C3 | 3.84 | 0.79 | 0.83 | 3.37 | 1.00 | 0.99 | 2.61 | 0.92 | 1.00 |
| F3 | 3.98 | 0.82 | 0.88 | 2.63 | 0.78 | 0.75 | 2.64 | 0.93 | 0.91 |
| E10 | 1.50 | 0.31 | 0.33 | 3.09 | 0.92 | 0.86 | 2.47 | 0.87 | 0.75 |
| F12 | 3.02 | 0.62 | 0.45 | 3.09 | 0.92 | 0.93 | 2.66 | 0.94 | 0.84 |
| C12 | 1.33 | 0.27 | 0.30 | 2.83 | 0.84 | 0.79 | 2.79 | 0.98 | 0.97 |
| C9 | 3.44 | 0.71 | 0.58 | 2.42 | 0.72 | 0.68 | 2.61 | 0.92 | 0.90 |

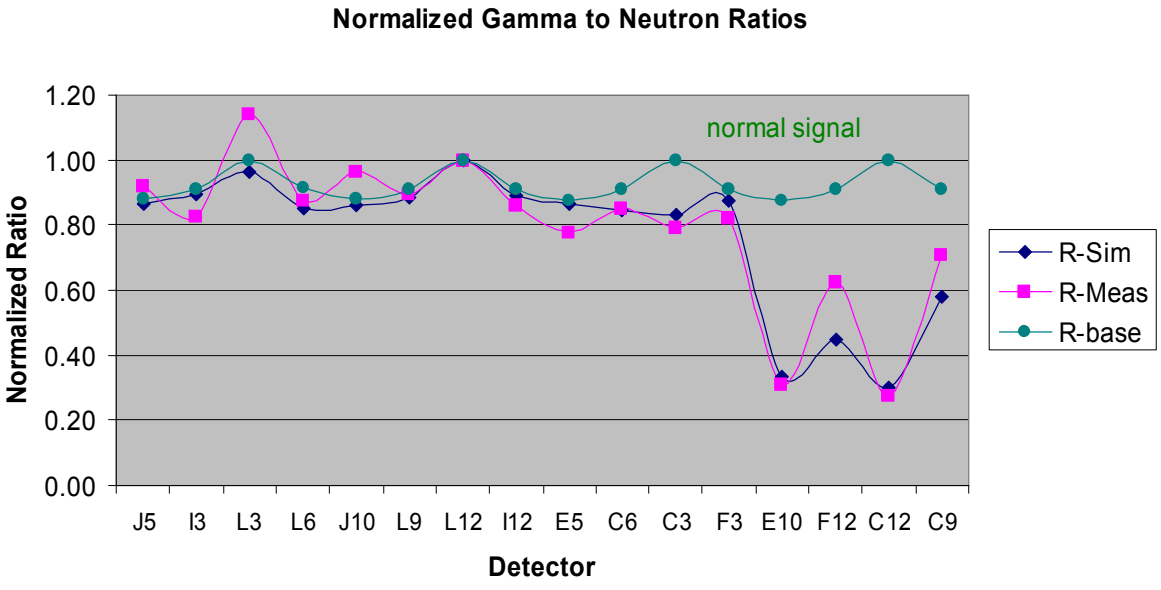


**Figure 44: Comparison of the experimental normalized ratio to MCNP simulated data for the assembly C15.**

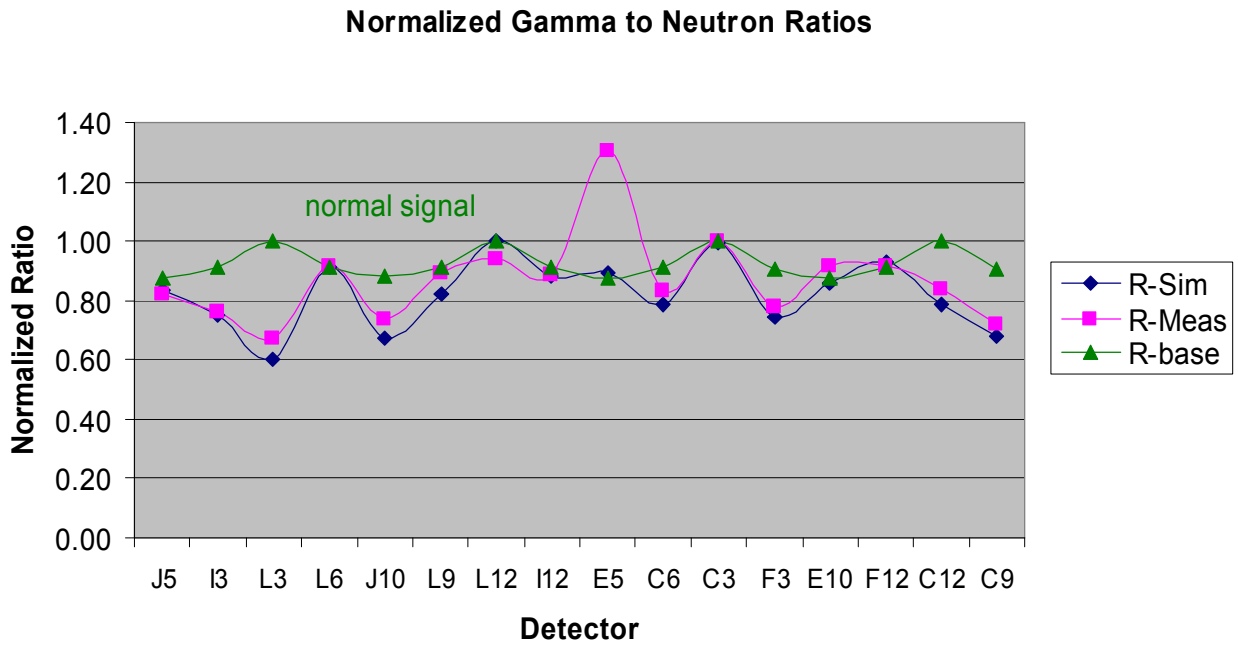


**Figure 45: Comparison of the experimental normalized ratio to MCNP simulated data for the assembly G23**

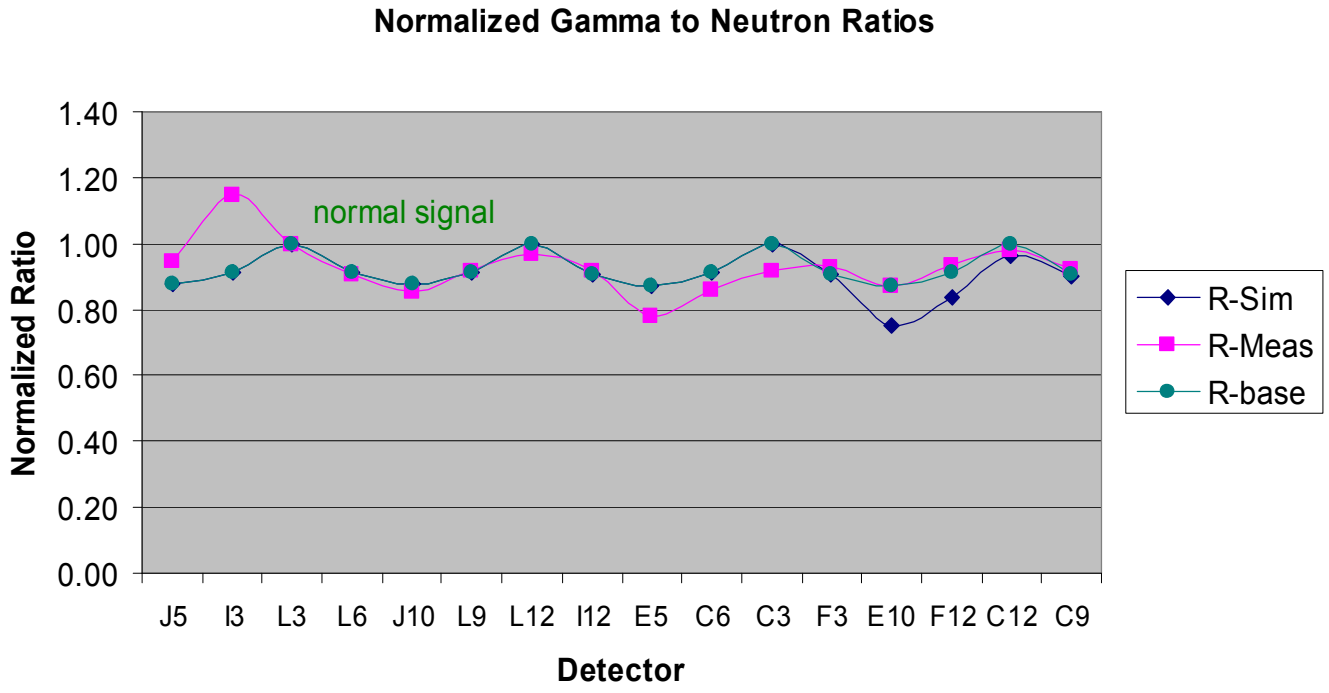


**Figure 46: Comparison of the experimental normalized ratio to MCNP simulated data for the assembly J14.**

## 13.0 CONCEPT OF A PRACTICAL FIELD DEVICE: PARTIAL DEFECT DETECTOR (PDET)

Having demonstrated a successful methodology for partial-defect verification for PWR spent fuel assemblies, the challenge is to design and fabricate a cost effective and field deployable practical device. As it is too cumbersome and time consuming to obtain measurements at each guide tube position one by one, the desired instrument should be able to obtain multiple signals from multiple detectors at the same time. This can be achieved by designing a multiple detector cluster (MDC) that contains multiple detectors so that simultaneous data acquisition is possible.

The conceptual MDC will have a main body and multiple rodlets connected to the main body of the MDC. Each rodlet will be a cylindrical container which holds a radiation detector. The rodlets of the MDC need to be inserted into guide tubes at the same time. As there are only a few types of PWRs in existence, an MDC can be designed for each. The envisaged shape of MDC would be something similar to Thimble Plug shown in Figure 47.

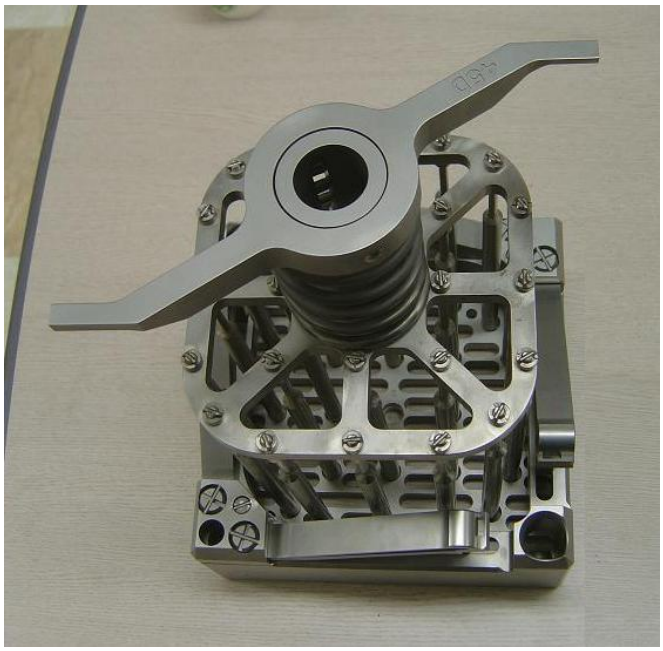

**Figure 47: A picture of Thimble Plug and a top nozzle for Westinghouse 17x17 PWR: The Thimble Plugs are used to control water flow through guide tubes of the spent fuel assemblies in a spent fuel pond. Similar to the Thimble Plug, the MDC will have a main body and multiple rodlets. Each rodlet will hold a radiation detector.**

The expected length of a rodlet would be approximately 125 cm. This is to ensure that the desired axial location for measurement inside the guide tube would be where the neutron or gamma flux is relatively flat.

One of the major elements that needs careful consideration in the design of MDC is the total number of detectors in the MDC and the method of data collection, as the total cost of the prototype can be quite high if a detector is placed at every rodlet. Taking advantage of the symmetric features of a PWR fuel assembly, full information can be obtained with limited number of detectors using a clever design of data acquisition and an optimal arrangement of detectors. For example, for the case of the Westinghouse 14x14 PWR assembly, a MDC with only 4 neutron detectors instead of 16 detectors can be used to obtain signals at every guide tube position. This would require four sets of measurements as the MDC rotates by 90 degree. As each measurement takes about 2 to 3 minutes, full information for an assembly will take no more than 15 minutes.

Further study into the design of PDET needs to be conducted to develop this simple yet powerful tool that can be deployed in the field.

## 14.0 CONCLUSION

A novel methodology to detect diversion of spent fuel from Pressurized Water Reactors (PWR) has been developed. The methodology makes use of inserting tiny neutron and gamma detectors into the guide tubes of a spent fuel assembly and measuring the signals. Simulation studies and a set of controlled experiments were performed and validated this novel methodology. Based on the simulation studies and benchmarking measurements undertaken during the course of this project, the methodology developed promises to be a powerful and practical way to detect partial defects that constitute 10% or more of the total active fuel pins. This far exceeds the detection threshold of ~50% missing pins, of the currently used FDET system. The methodology does not rely on any operator provided data like burnup or cooling time and does not require movement of the fuel assembly from the storage rack in the spent fuel pool.

The proposed instrument, Partial Defect Detector (PDET), has the potential of being a powerful and practical tool for use in the field in a minimally intrusive manner and without relying on any operator provided data on the spent fuel assemblies. The PDET promises to be a breakthrough in partial defect detection technology, and an answer to this long unsolved safeguards technical problem.

## 15.0 REFERENCES


1. B. D. Murphy and P. De Baere, “Monte Carlo Modeling of a Fork Detector System,” 27th Annual Meeting, Symposium on Safeguards and Nuclear Material Management, London, England, May 10–12, 2005.
2. Titta, et. al, “Investigation on the possibility to use FORK detector for partial defect verification of spent LWR fuel assemblies, Final report on Task JNT A 1071 of the Member State’s Support Programme to IAEA Safeguards, 2002.
3. F. Levai, et al, “Feasibility of gamma emission tomography for partial defect verification of spent LWR fuel assemblies,” Task JNT 1201 of the Finland, Hungary and Sweden to the IAEA safeguards, 2002.

4. ORIGEN-ARP, Versions 5.0/5.1.01, Isotope Generation and Depletion Code, CCC-725/732, Radiation Safety Information Computational Center, May 2004/March 2007.
5. S.P.Cerne, O.W.Hermann, R.M. Westfall, "Reactivity and Isotopic Composition of Spent PWR Fuel as a Function of Initial Enrichment, Burnup, and Cooling Time", ORNL/CSD/TM-244, Oakridge National Laboratory, October 1987.
6. X5-Monte Carlo Team, MCNP-A general Monte Carlo N-Particle Transport Code, Version 5.1.40, Los Alamos National Laboratory, February 2006.
7. Private Communication from KAERI.
8. J.R.Phillips, "Irradiated Fuel Measurements", in "Passive Nondestructive Assay of Nuclear Materials", NUREG/CR-5550, edited by D. Reilly et. al., March 1991.
9. Y. Ham, G. I. Maldonado, C. Yin, J. Burdo, "Monte Carlo Characterization of Pressurized Water Reactor Spent Fuel Assembly for Development of a New Instrument for Pin Diversion Detection," Institute of Nuclear Materials Management 47th Annual Meeting, Nashville, TN, July 2006.
10. Y. Ham, G. I. Maldonado, J. Burdo, T. He "Development of a Safeguards Verification Method and Instrument to Detect Pin Diversion from PWR Spent Fuel Assemblies," Symposium on International Safeguards, Vienna, Austria, 16-20 October, 2006
11. S. Sitaraman and Y.S. Ham, "Characterization of a Safeguards Verification Methodology to Detect Pin Diversion from Pressurized Water Reactor (PWR) Spent Fuel Assemblies using Monte Carlo Techniques", 48th Annual Meeting of the Institute of Nuclear Materials Management, Tucson, AZ, July 2007.
12. OECD/NEA Spent Fuel Database: http://www.nea.fr/sfcompo/
13. S. Sitaraman and Y.S. Ham, "Sensitivity Studies for an In-Situ Partial Defect Detector (PDET) in Spent Fuel using Monte Carlo Techniques", 49th Annual Meeting of the Institute of Nuclear Materials Management, Nashville, TN, July 2008.